



28 **1. Introduction**

29 Deep injections of tens to hundreds of keV particles into the inner magnetosphere, i.e. drift shells
30 $L < 6$, during quiet geomagnetic conditions or weak storm activity have recently become one of
31 the main issues of radiation belt dynamics (e.g., Turner et al., 2017a; Zhao et al., 2017a). The
32 cause of “quiet” injections has not been understood yet. An injection depth is estimated using a
33 notion of drift L-shell, defined by McIlWain (1961). The L parameter determines the unique drift
34 shell, which remains constant when a charged particle moves adiabatically in the inner
35 magnetosphere. Numerically, L gives the average geocentric distance to a drift shell at the
36 magnetic equator. Injection or transport of particles implies violation of adiabatic motion and
37 changing of L-shell.

38 The mechanisms responsible for the violation of adiabatic motion of energetic particles are a
39 subject of extensive modern studies of the radiation belts (e.g., Turner et al., 2015; Turner et al.,
40 2017b; Zhao and Li, 2013; Zhao et al., 2016; Zhao et al., 2017a). The studies presented some
41 intriguing challenges for current models of energetic particle injections in L-shell range of 2-6.
42 Particularly it was pertaining to discrepancy in occurrence frequency, energy range, local time
43 and penetration depth of electron versus proton injections. Zhao et al. (2016) showed that the
44 electrons penetrate into the low L-shells more frequently than protons. In addition, it was found
45 that tens to hundreds of keV electrons penetrate deeper than MeV energy electrons (e.g., Zhao
46 and Li, 2013; Zhao et al., 2016). It was also found that energetic electrons can often penetrate
47 down to the slot region separating the inner and outer radiation belts ($L \sim 2.5 - 3.5$) and also into
48 the inner radiation belt at $L < 2$. Moreover, the deepest penetrations of energetic electrons were
49 revealed even under the inner radiation belt at $L < 1.2$ (Asikainen and Mursula, 2005; Evans,
50 1988; Suvorova et al. 2012; 2013).

51 In the recent study, Zhao et al. (2017a) have compared local time characteristics of electron and
52 proton flux enhancements in the slot region and suggested that underlying physical mechanisms
53 responsible for deep penetrations of protons and electrons are different. Particularly, deep proton



54 penetration is consistent with convection of plasma sheet protons, and deep electron penetration
55 suggests the existence of a local time localized mechanism. Turner et al. (2015) studied energetic
56 electron flux enhancements at $L < 6$ and also suggested that the deep injections at $L < 4$ (inside
57 the plasmasphere) may result from a different mechanism than injections observed at higher L
58 shells (outside the plasmasphere). They hypothesized that the mechanism could be related to
59 wave activity in the Pi2 frequency range which usually serves as an indicator of substorm
60 activity. Overall, dynamics of the tens to hundred keV electrons at low L -shells is very different
61 from dynamics of both protons and electrons at higher L -shells and also in higher energy range.

62 The ability of energetic electrons to penetrate deeply in the inner zone and below is still puzzling.
63 An answer to the question may be found by investigating the relation of deep injections of
64 energetic electrons to solar wind parameters, geomagnetic activity indices and other parameters
65 of magnetospheric and ionospheric responses (Suvorova, 2017; Zhao et al., 2017b). The studies
66 mentioned above have reported deep injections of energetic electrons associated with
67 geomagnetic storms and/or intense substorms, although no significant dependence of penetration
68 depth or flux intensity on the storm intensity was found (e.g., Suvorova et al., 2013; 2014;
69 Turner et al., 2017b; Zhao et al., 2016). Some studies noted that deep injections can occur during
70 nonstorm time but under intense substorm activity (Park et al., 2010; Suvorova et al., 2016;
71 Turner et al., 2015).

72 Extensive studies of dynamics of the energetic electrons in the inner radiation belt and below
73 using the measurements from several satellite missions NOAA/POES, DMSP, DEMETER, and
74 Van Allen Probes (e.g., Reeves et al., 2016; Suvorova, 2017; Turner et al., 2015, Turner et al.,
75 2017a; Zhao and Li, 2013; Zhao et al., 2017a) have revealed the following interesting features
76 such as a high growth rate of fluxes or sudden enhancements, the occurrence of flux
77 enhancements regardless of storm intensity, the influence of solar wind and geomagnetic
78 conditions on the occurrence rate, high occurrences of the injections below the inner zone during
79 specific phases of solar cycles, specific months and local times.



80 Rapid enhancements of electron fluxes in the inner zone have been known for a long time in
81 association with deep injections of particles during strong magnetic storms (e.g., Pfitzer and
82 Winckler, 1968; Imhof et al. 1973; Kikuchi and Evans, 1989; Tanaka et al., 1990). As mentioned,
83 recent studies showed that rapid or sudden enhancements deep in the inner magnetosphere
84 cannot be explained by an enhanced convection electric field, convection of plasma sheet
85 electrons or inward radial diffusion (e.g., Turner et al., 2017b; Zhao et al., 2017a). Increased
86 statistics have revealed a feature that deep injections may occur frequently, and furthermore,
87 regardless of storm strength (Tadokoro et al., 2007; Park et al., 2010; Turner et al., 2017a; Zhao
88 and Li, 2013; Zhao et al., 2016). Another important feature, also mentioned above, is that
89 injections of the keV electrons and associated flux enhancements can occur even below the inner
90 belt edge ($L \sim 1.2$), in so-called forbidden zone (Asikainen and Mursula, 2005; Evans, 1988;
91 Suvorova et al., 2012).

92 Until recent years, it was believed that these “forbidden injection” events could occur only
93 during strong magnetic storms and hence could be rarely observed. Note that enhancements in
94 the forbidden zone were first reported in 1960s (Krasovskii et al., 1961; Savenko et al., 1962;
95 Heikilla, 1971), however, the conclusions were unconvincing due to the scarce information (see
96 Paulikas, 1975 for a review). The recent statistical study of electron enhancements in the
97 forbidden zone showed that the injections below the inner zone can also occur during
98 geomagnetically quiet conditions (Suvorova, 2017). This fact is consistent with the recent
99 finding of “quiet” injections in the inner magnetosphere (Turner et al., 2017a; Zhao et al., 2017a).
100 A case of “quiet” injections of energetic electrons at $L < 1.2$ is in the focus of our study.

101 Here, we summarize the main characteristics of the electron injections into the very low L-shells
102 from several papers (Suvorova and Dmitriev, 2015; Suvorova et al., 2013; 2014; 2016; Suvorova,
103 2017; Dmitriev et al., 2017). The quasi-trapped energetic electron population in the forbidden
104 zone, referred to as forbidden energetic electrons (FEE), can be characterized as transient with
105 highly variable fluxes. The behavior of FEE is similar to keV energy trapped electrons in the



106 inner radiation belt with flux enhancements in response to magnetic storms (e.g., Kikuchi and
107 Evans, 1989; Tanaka et al, 1990; Tadokoro et al., 2007; Dmitriev and Yeh, 2008; Zhao and Li,
108 2013; Selesnick et al., 2016). Simultaneous measurements of particles by satellites at different
109 altitudes provided clear evidence that the forbidden zone enhancements of energetic electrons
110 were caused by fast penetration of the inner belt electrons (Suvorova et al., 2014). As known, an
111 important role in fast transport of particles during storms is played by magnetic and electric field
112 perturbations. Such perturbations are usually associated with the influence of magnetospheric
113 substorms, or nighttime processes of magnetic field dipolarizations in the magnetotail (e.g.,
114 Glocer et al., 2011; Selesnick et al., 2016). However, substorm signatures in the magnetic field in
115 the low- L region ($L < 2$) have never been observed.

116 Thus, the deep injections of keV energy electrons may extend even to the forbidden zone, but
117 conditions for the fast ($\sim 1 - 2$ h) earthward transport in the low- L region are still unclear.
118 Nevertheless, the most probable mechanism of the low- L injections of energetic electrons was
119 suggested as the $E \times B$ drift (e.g., Suvorova et al., 2012), and most of researchers consider and
120 model an electric drift of electrons in the $E \times B$ fields, even though the electric field must be very
121 high (e.g., Zhao and Li, 2013; Turner et al., 2015; Lejosne and Mozer, 2016; Selesnick et al.,
122 2016; Su et al., 2016; Zhao et al., 2017a). There is no explanation for penetration of a strong
123 electric field to such low L -shells. What is more important, there is no reliable information on
124 electric fields at heights of 500-2000 km, because measurements there are difficult, and, as a
125 consequence of this, empirical electric field models are limited and do not provide the results
126 below $L \sim 2$ (e.g., Rowland and Wygant, 1998; Matsui et al., 2013). The most modern research
127 suggests that the actual strength of penetration electric fields can be stronger than any existing
128 electric field model at $L < 2$ (Su et al., 2016).

129 The studies, mentioned above, have also analyzed a relation between the FEE injections and
130 geomagnetic activity level. It seemed for a while that intense geomagnetic activity like auroral
131 substorms was one of the necessary factors for deep electron injections, and the storm-time Dst -



132 variation did not control the FEE occurrences (Suvorova et al., 2014). It was suggested that
133 substorm-associated strong electric field can penetrate to the low L region, thereby creating the
134 conditions for fast earthward transport of trapped electrons in crossed E and B fields. Recent
135 modeling of the ExB transport mechanism at $L < 1.3$ demonstrated that the mechanism can
136 successfully operate in the low L region (Selesnick et al., 2016).

137 However, after that, many FEE events were found during moderate and weak auroral activity,
138 which was typical for pre-storm (initial phase) or even non-storm conditions (Suvorova and
139 Dmitriev, 2015; Suvorova et al., 2016). Thus, though no evidence of direct influence of
140 geomagnetic storms was found, the FEE enhancements appeared to be necessarily associated
141 with substorm activity in some events studied (Suvorova et al., 2014; 2016). However,
142 statistically, such a casual relationship with substorms was not confirmed (Suvorova, 2017).
143 From total statistics of ~530 days with FEE enhancements collected during two solar cycles
144 (Suvorova, 2017), we found more than three dozen days without essential substorm activity.
145 These “quiet” events occurred over past decade from 2006 to 2016. The FEE enhancements in
146 that case were observed only in low energy range of tens of keV.

147 It is important to mention that one interesting feature was unexpectedly found from the statistical
148 study (Suvorova, 2017). It is that the most favorable conditions for the FEE enhancements arise
149 in the period from May to September independently on geomagnetic activity level. A second,
150 minor peak of occurrence appears in the December - January period. Suvorova (2017) suggested
151 an important role of the auroral ionosphere in the occurrence of FEE injections. The peculiar
152 annual variation of the FEE occurrence rate was explained by a change in conductance of the
153 auroral ionosphere. The conductance depends directly on the illumination of the noon sector of
154 the auroral zone. As known, the high-latitude ionosphere is better illuminated during solstice
155 periods, with that the illumination of the northern region is higher than the illumination of the
156 southern one because of the dipole axis offset relative to the Earth’s center. This fact can explain



157 an existence of two peaks of the FEE occurrence with the major one during the northern summer
158 period.

159 The factor of auroral ionosphere conductivity is necessary but not sufficient, and it comes to the
160 fore during weak geomagnetic activity. External drivers from the solar wind should trigger some
161 processes in the magnetosphere-ionosphere system that can result in the electron injections into
162 the forbidden zone. What are these processes when storm and substorm do not develop is still
163 unclear. A comprehensive analysis of the solar wind drivers and magnetospheric response may
164 help us to lift the veil. In this paper, we study prominent FEE enhancements during nonstorm
165 condition on August 1, 2008 in order to determine their possible drivers in the solar wind.

166

167 **2. Observations on August 1, 2008**

168 **2.1. Forbidden Electron Enhancements**

169 Figure 1 shows large enhancements of the >30 keV electron fluxes at low latitudes on August 1,
170 2008. The data were compiled from all orbital passes of five NOAA/POES satellites. The
171 electron fluxes in the energy ranges >30, >100 and >300 keV were measured by the MEPED
172 instruments boarded on each satellite. The MEPED instrument includes two identical electron
173 solid-state detector telescopes and measures particle fluxes in two directions: along and
174 perpendicular to the local vertical direction (Evans and Greer, 2004). The data shown in Figure 1
175 are from the detector was oriented along the orbital radius-vector, so that it measured quasi-
176 trapped particles near the equator and precipitating particles in the auroral region. In Figure 1,
177 the forbidden zone extends in the latitudinal range from -20° to $+30^\circ$ and in the longitudinal
178 range from 0° to 260°E (or 100°W) that is beyond the South Atlantic anomaly (SAA) at $L < 1.2$.
179 Figure 1a shows the observations of the >30 keV electrons at 0-12 UT, before the enhancements
180 occurred. Figure 1b shows the interval 12-24 UT, when fluxes of >30 keV quasi-trapped
181 electrons in the forbidden zone increased by 3 orders of magnitude above a background of $\sim 10^2$
182 $(\text{cm}^2 \text{ s sr})^{-1}$ and kept at the enhanced level for several hours. As found previously, the flux



183 enhancements at low latitudes are peculiar to the quasi-trapped energetic electrons (Suvorova et
184 al., 2012, 2013). In contrast, enhancements of electrons precipitating at low latitudes are very
185 rare, weak and short. During the event, precipitating electron fluxes in the forbidden zone did not
186 increase (not shown). Fluxes of the >100 keV electrons and >30 keV protons did not increase
187 also (not shown). The quasi-trapped electrons are mirroring at heights below the satellite orbit
188 (~850 km) in a region of $\pm 30^\circ$ latitudes, and drift eastward with a rate of 17° - 19° per hour toward
189 the SAA area, where they are lost due to scattering in the dense atmosphere.

190 Figure 2 and Table 1 present longitudinal and local time locations of 15 FEE enhancements
191 detected at equatorial passes of POES satellites (P2, P5, P6, P7, P8). Positions of the satellite
192 orbital planes provided a good coverage of the entire local time (LT) range: 9 - 21 LT (P2 and
193 P7), 5 - 17 LT (P5 and P6), and 2 - 14 LT (P8). The coverage allows determining the injection
194 region with uncertainty of approximately 2 h. The first FEE enhancement was observed at ~1250
195 UT in Central Pacific at night time (2 LT), and the last (enhancement number F15) was detected
196 at ~2310 UT near the western edge of SAA at day time (17 LT).

197 It was shown statistically that deep injections into the forbidden zone, similar to plasma sheet
198 particle injections, occur in the midnight - morning sector (e.g., Suvorova, 2017). During typical
199 geomagnetic disturbances, nighttime FEE enhancements are observed shortly after local
200 injections and near an injection site, while subsequent FEE enhancements at daytime are already
201 the result of azimuthal drift of electrons injected on the nightside. Hence, the nighttime (~2 LT)
202 enhancements F1 and F4 of >30 keV electron fluxes indicate approximately the time of injection,
203 respectively, at ~1250 and ~1430 UT or a little bit earlier. After 1530 UT, enhancements were
204 observed at daytime (numbers F7, F9, and F11-15) and are therefore associated with drifting
205 electrons.

206 All remaining enhancements F2, F3, F5, F6, F8 and F10 of >30 keV electron fluxes were
207 observed in the early morning (5 LT) for a long time interval of ~4 h that lead us to suspect that
208 the enhancements were observed near the injection site. Nevertheless, we examine the



209 assumption about drift by comparing these enhancements with the injection time for numbers 1
210 and 4 in Table 1. For the enhancements F1 and F2, 30 keV electrons injected at 1250 UT must
211 drift $\sim 35.4^\circ$ of longitude in order to reach the observing satellite P5. It takes ~ 112 min with the
212 drift rate of $19^\circ/\text{h}$ for 30 keV electrons at $L \sim 1.2$ or 125 min with the drift rate of $17^\circ/\text{h}$ at $L \sim 1.1$.
213 However, the observed time difference between F1 and F2 is only 25 min that is too short for
214 drifting from the longitude of F1 to the longitude of F2.

215 The enhancements F1 and F3 have the longitudinal difference of 26° for 1 h that is much larger
216 than 19° produced by the drift of >30 keV electrons. Either it could be electrons of slightly
217 higher energy of $\sim 40\text{-}50$ keV. However, intensity of these electrons is several times lower than
218 that for 30 keV electrons because of very steep energy spectrum with maximum in the range of
219 $20\text{-}30$ keV as shown in the previous study (Suvorova et al., 2013). In contrast, the observations
220 did not show notable flux decrease. It means that vast majority of the POES/MEPED count rate
221 is produced by electrons of ~ 30 keV.

222 Likewise, one can infer that the enhancement F4 also did not result in the enhancements F5 and
223 F6 and certainly not in the enhancements F8 and F10. Therefore, the specific longitudinal and
224 local time distributions of the enhancements indicate multiple injections during about 4.5 h in the
225 sector of $0 - 6$ LT, and the injection region was confined within 3 h of local time over central and
226 eastern Pacific. In general, these characteristic of injections are in well agreement with those
227 found from statistics (Suvorova, 2017).

228

229 **2.2. Upstream Solar Wind Conditions**

230 An intriguing aspect of these FEE injection events is that they occurred under quiet, nonstorm
231 conditions, characterized by $Dst/SYM\text{-}H \sim 0$ nT and $AE < 100$ nT. We examine solar wind
232 parameters to search for drivers inducing such deep electron injections. In the study, we focus on
233 a comparison between the solar wind parameters measured far upstream and near the bow shock



234 and on their influence on the magnetospheric magnetic field during the period of interest. Global
235 indices of geomagnetic activity and solar wind data from the Omni high-resolution data set are
236 shown in Figure 3. The OMNI data base provides solar wind data, which were originally
237 obtained from upstream monitors (e.g., ACE or Wind satellites) near the L1 libration point at
238 geocentric distance of $\sim 230 R_E$ (R_E is the Earth's radius), and then the data were corrected by
239 time delay procedure due to propagation to the Earth's bow shock (King and Papitashvili, 2005).

240 As seen in Figure 3, the solar wind speed and density smoothly varied around averages of 400
241 km/s and 6 to 4 cm^{-3} , respectively, that resulted in gradual change of the dynamic pressure from
242 2 to 1 nPa. The interplanetary magnetic field (IMF) can be characterized as weakly disturbed by
243 small-scale structures because of chaotic variations of the magnetic field components and
244 discontinuities, particularly during the first half of the day. Also, in this period, the B_z component
245 was predominately positive. Later, there was a short interval from 1500 to 1800 UT, when IMF
246 orientation was relatively steady with a continuous negative B_z of about -2 nT. Likely, the
247 southward IMF resulted in intensification of the AL index from 16 to 18 UT with a peak of -250
248 nT. The 1 min $SYM-H$ index was > -10 nT throughout the whole day, indicating there was no
249 geomagnetic storm. Therefore, the solar wind conditions resulted in a weak auroral disturbance
250 like an isolated substorm.

251 Overall, the OMNI magnetic and plasma parameters can be characterized as almost undisturbed
252 in the period of the FEE enhancements from 1200 to 2300 UT. Obviously, the weak auroral
253 activity at ~ 1700 UT could not result in extremely deep injections of the energetic electrons,
254 which started much earlier, around 1300 UT. Whereas, looking on the PC index, which
255 represents magnetic activity in the northern (PCN) and southern (PCS) polar caps (Troshichev et
256 al., 1988), one can see a clear disturbance, particularly in the northern polar cap, in the period
257 from 1300 to 1530 UT. But it's difficult to identify appropriate solar wind drivers for
258 interpretation of this polar cap activity.



259 This raises the question of actual solar wind characteristics at the near-Earth location during the
260 event. The FEE enhancement event under the nonstorm condition and mild, ordinary solar wind
261 properties presents intriguing challenge to current understanding of the deep energetic particle
262 injections, which usually are associated with intense substorm activity. From the characteristic
263 PC-index behavior, we suspect the actual solar wind parameters affecting the magnetosphere
264 may be different from those predicted by OMNI. Fortunately, the near-Earth THEMIS mission
265 can provide necessary reliable information on upstream conditions.

266

267 **2.3. THEMIS foreshock observations**

268 During the time interval from 1200 to 1800 UT, the THEMIS-C satellite (TH-C) had a position
269 upstream of the bow shock in the subsolar region (Figure 4). The TH-C probe moved from
270 location (17.2, -0.3, -5.9) Re in GSM at 1200 UT to location (18.1, 3.4, -5.9) Re at 1800 UT.
271 Hence, we can evaluate characteristics of the upstream solar wind structures actually affecting
272 the magnetosphere during the period of the FEE enhancements. Figure 5a shows measurements
273 of the THEMIS-C/FGM fluxgate magnetometer in GSM coordinates with a time resolution of ~3
274 s (Auster et al., 2008) and the ion spectrograms from THEMIS-C/ESA plasma instrument
275 (McFadden et al., 2008). The magnetic field components measured in situ by TH-C are
276 compared with those predicted by OMNI and shown in Figure 5b. Also, Figure 5c presents the
277 IMF cone angles, between the IMF vector and the Earth-Sun line, for both magnetic data sets.

278 From 1200 UT to 1320 UT, three TH-C magnetic components demonstrated small-amplitude
279 variations, and the Bz component had northward direction. During this time, there were
280 discrepancies between magnetic components of the TH-C and OMNI data caused mostly by time
281 shift of ~10-15 min, so that TH-C observed arrival of the solar wind structures at earlier time
282 than that predicted by OMNI. With time correction, one can achieve better consistency in the
283 two magnetic data sets except the difference in the Bx components about 1310 UT.



284 In Figure 5c, the OMNI cone angle dropped below 30° between 1330 and 1520 UT that
285 corresponded to quasi-radial IMF orientation (IMF is almost along the Earth-Sun line), whereas
286 cone angle variations detected by TH-C were very different from the OMNI data. After 1500 UT,
287 the OMNI data do not match the TH-C observation any more, even with time correction. About
288 ~ 1320 UT, ~ 1400 UT and after 1440 UT, the in-situ observation of THEMIS shows large-
289 amplitude fluctuations with duration of tens of minutes in three magnetic components and cone
290 angle (Figure 5a, c). The observed large magnetic fluctuations are ultralow-frequency (ULF)
291 waves, and they are a typical signature of the upstream region of quasi-parallel bow shocks, so-
292 called foreshock (e.g., Schwartz and Burgess, 1991). In addition, in the same time intervals, the
293 plasma spectrogram shows enhancements of suprathermal ion fluxes with energy of >10 keV
294 (upper panel in Figure 5a). This is another distinguishing signature of the foreshock, known as
295 diffuse ion population, which is always observed together with the upstream ULF waves
296 (Gosling et al., 1978; Paschmann et al., 1979; Greenstadt et al., 1980; Crooker et al. 1981).
297 Hence, the upstream foreshock waves and diffuse ions observed by TH-C in the subsolar region
298 are associated distinctly with a radial or quasi-radial IMF orientation in the undisturbed solar
299 wind. Note, that the longest foreshock interval (1435 - 1550 UT) associated with the quasi-radial
300 IMF orientation was observed by ~ 20 min later than that predicted by OMNI.

301 After 1520 UT, the prediction and in-situ data mismatch greatly. The TH-C satellite observed
302 several rotational discontinuities and alternation between Archimedean spiral and radial
303 orientations of the IMF vector, while the OMNI magnetic field does not change the Archimedean
304 spiral orientation from 1520 to 1740 UT. The foreshock returned to the subsolar region
305 periodically and more frequently in the interval 1600 - 1730 UT than in the earlier period 1320 -
306 1440 UT.

307 These two time intervals of frequent foreshock transitions differ in the B_z component: $B_z > 0$ at
308 1320 - 1440 UT and $B_z < 0$ at 1600-1700 UT. It's natural, that the southward B_z results in the
309 weak auroral activity during the later interval. Nevertheless, the changing direction of IMF has



310 the effect on the magnetic activity in the northern polar cap in the both interval (see the PC index
311 in Figure 1). We check available satellite and ground-based magnetic data to find other responses
312 inside the magnetosphere to the foreshock transitions.

313

314 **2.4. Magnetospheric magnetic field perturbations**

315 We use magnetic field and plasma measurements in the magnetosphere from the other three
316 THEMIS probes and GOES-12 satellite in order to find signatures of local magnetospheric
317 disturbances. With these data, we examine a magnetospheric response to the subsolar foreshock,
318 which forms each time with arrival of magnetic flux tubes with quasi-radial IMF orientation.
319 Positions of the TH-B, TH-D, TH-E and GOES-12 satellites in the X-Y GSM plane for the
320 period from 1200 to 1800 UT are shown in Figure 4. We used the model of Lin et al. (2010) to
321 calculate magnetopause position. The OMNI data at 1600 UT is used as input data for the model.
322 The GOES12 satellite moved from morning to noon (7 - 13 LT). The TH-E and TH-D probes
323 moved outward from prenoon to postnoon, and the TH-B probe moved inward in the afternoon-
324 dusk sectors.

325 Figure 6 shows variations of the Bz component measured by the TH-E, TH-D, and TH-B probes,
326 the magnetic field strength at geosynchronous orbit (GOES-12), the ion spectrogram from the TH-
327 D satellite and the SYM-H index from 1200 to 1800 UT. As seen in Figure 6 (a, d),
328 characteristics of magnetic field and hot plasma indicate that three THEMIS probes were located
329 inside the dayside magnetosphere during the interval, a region of a strong magnetic field with the
330 magnitude ranging from 40 to 150 nT and low-density of hot (>10 keV) ions. Three THEMIS
331 probes observed significant perturbations in the magnetic field Bz component with
332 increase/decrease of order of several to tens of nT. After 1400 UT, the largest amplitudes were
333 observed by TH-D, which was closer to the magnetopause than other probes at that time (see
334 Figure 4). From 1300 to 1500 UT, there are a few characteristic decreases and enhancements in
335 the Bz component with duration of 20-30 min observed by all probes (Figure 6a). The magnetic



336 field increases correspond to magnetospheric compressions, and the decreases are
337 magnetospheric expansions (e.g., Dmitriev and Suvorova, 2012). Prominent magnetic peaks are
338 indicated by dashed lines and listed in Table 2. At ~1700 and 1715 UT, the TH-D measurements
339 show that the sign of the B_z component suddenly reversed for a few minutes. The negative B_z
340 component is a clear signature of the magnetosheath magnetic field. We will consider details of
341 the magnetosheath intrusion events later.

342 As seen in Figures 6a-c, THEMIS magnetic observations well correlate with magnetic field
343 variation observed by GOES-12 and with the SYM-H index in the interval 1300-1600 UT. The
344 first magnetic pulse was observed at ~13:33:40 simultaneously by TH-B, TH-E, and TH-D and
345 with a delay of ~2 min by GOES 12. Time moments of magnetic peak 2 coincide for all satellites
346 (14:20:50 UT). Magnetic peak 3 was observed at first by GOES 12 at ~15:44:00 (~10.6 LT),
347 then by TH-E at ~15:47:30 (~12 LT) and at last by TH-D at ~15:50:30 UT (~12.5 LT), so a time
348 difference between GOES 12 and TH-D is ~ 6.5 min and between TH-E and TH-D is 3 min.

349 The magnetic variations associated with compression-expansion effects could not be caused by
350 the solar wind pressure variations, which were gradual and small during the interval (see Figure
351 3). However, the magnetic perturbations may result from local variations in the magnetosheath
352 pressure. Unfortunately, THEMIS did not measure plasma parameters in the magnetosheath from
353 1200 to 1600 UT, but an analysis of the later interval (1600-1800 UT) can provide important
354 information about magnetosheath conditions (see also section 2.5).

355 After 1545 UT, the TH-D probe observed fast magnetic variations. At that time the probe was
356 approaching the magnetopause and moving ahead of the TH-E probe (see Figure 4). Note, that
357 the fast magnetic fluctuations are not always seen in SYM-H and GOES 12 data because of a
358 low time resolution (1 min) of these data. Figure 6d presents the ion spectrogram from TH-D.
359 One can see several short-time intrusions of dense and cold plasma with spectrum typical for the
360 magnetosheath. Moreover, at ~1700 and 1710 UT, the magnetospheric field measured by TH-D
361 with positive B_z suddenly overturned to negative B_z for a moment that indicated a



362 magnetosheath encounter. Time moments of peaks in the magnetosheath plasma pressure are
363 indicated by lines 4-10 in Figure 6 and listed in Table 2. Below, we analyze characteristics of
364 magnetosheath ions in details.

365

366 **2.5. Magnetosheath plasma jets interacting with the magnetopause**

367 We analyze the solar wind characteristics in the foreshock region together with the
368 magnetospheric magnetic perturbations and penetration of magnetosheath ions. Figure 7 shows
369 the magnetic field and plasma parameters observed by TH-D, TH-E and TH-C during the
370 interval 1530-1800 UT. In addition, magnetic measurements from GOES 12 and geomagnetic
371 indices are also shown.

372 After 1530 UT, the TH-D and TH-E probes have observed magnetic field pulses associated with
373 the compression effect (Figure 7g). After 1600 UT, TH-D was approaching the magnetopause
374 and started observing occasionally magnetosheath plasma in the magnetosphere, as seen in the
375 ion spectrogram (e.g., lines #4 – 7 and 10, Figures 7b). After 1700 UT, the probe twice entered
376 into and exited from the magnetosheath region as indicated by lines #8 and #9. The
377 magnetosheath plasma can be recognized as dense and cold (<1 keV) ion population. As seen in
378 Figure 7 (panels b and g), not all magnetic pulses are accompanied by plasma penetrations.
379 During the interval, the outermost probe TH-C observed occasionally the foreshock phenomena
380 such as diffuse ions (≥ 10 keV) in the spectrum (panel a) and large IMF cone angle fluctuations
381 associated with ULF waves (panel h). As one can see, most of the magnetic pulses (panel g)
382 and/or magnetosheath ion populations (panel b) indicated by lines #3, #4, and #6-10 (i.e. except
383 #5) were accompanied by the foreshock diffuse ions (panel a).

384 Figure 8 shows characteristics of magnetosheath plasma in details for three intervals 1600-1630,
385 1630-1700, and 1658-1728 UT. Since plasma charge neutrality means equal density of ions and
386 electrons, Figure 8 presents parameters of the ion component only (panels a-d). Dynamic



387 pressure and density of the solar wind plasma measured far upstream by the ACE monitor are
388 also shown for comparison in panels (b, c). The time period from 1600 to 1630 UT is shown in
389 panels (a1-g1). The probes TH-D and TH-E observed magnetic field variation in specific
390 depletion-hump sequence from 1607 to 1614 UT (panels f1, g1), similar to the variations
391 indicated by lines #1 - #3 in the earlier interval (see Figure 6). Magnetic peak is indicated by line
392 #4. Additionally, wave-like structures with a period of ~30-60 sec (in the ULF range) are clearly
393 seen in magnetic measurement of both probes during the time interval from 1609 to 1627 UT
394 (panels f1, g1). At 1614 - 1616 UT, TH-D observed cold ions (~100 eV - 3 keV) and electrons
395 (<1 keV, not shown) of the magnetosheath origin staying in the magnetosphere (panel a1). The
396 plasma has maximal speed of >200 km/s and high density of 3-9 cm⁻³ that result in the high total
397 pressure of 1.5 - 1.8 nPa (panels b1-d1). Its dynamical characteristics distinctly exceed the solar
398 wind parameters with density of 4 - 5 cm⁻³ and total pressure of ~1.1 nPa (panels b1, c1). Internal
399 structure of plasma forms 3 prominent pressure pulses between 16:14:50 and 16:16:00 UT, a
400 central pulse is dominated by magnetic component (panel f1) and two lateral pulses are
401 dominated by dense plasma components (panel c1). Two plasma density enhancements produced
402 a diamagnetic effect seen as a characteristic decrease of magnetic field (panel f1). At the outer
403 edge of the plasma structure, the anti-sunward velocity ($V_x < 0$) reached high value of -100 km/s,
404 indicating that the local plasma flow struck and interacted with the magnetopause (panel d1).
405 The V_z component demonstrates a maximal value in southward direction (-200 km/s). Three
406 rotated velocity components V_x , V_y and V_z indicate that vortex-like plasma structure propagated
407 along the magnetopause toward south and dusk. This dense and high-speed plasma structure is
408 analogous to the large-scale magnetosheath plasma jet studied by Dmitriev and Suvorova (2012).
409 Large-scale magnetosheath plasma jets are defined as intense localized fast ion fluxes whose
410 kinetic energy density is several times higher than that in the upstream solar wind and duration is
411 longer than 30 sec (Dmitriev and Suvorova, 2015).



412 Panels (a2-g2) in Figure 8 show magnetic compressions and magnetosheath penetrations (lines
413 #5 - #7) during the time period from 1630 to 1700 UT. It is also seen that the magnetic field
414 measured by TH-E was disturbed by ULF wave activity (panel g2). The plasma structures #5 and
415 #6 (panel a2) have short durations and are characterized by extremely high density of 16 and 12
416 cm^{-3} , respectively, that well explain the compression effects in magnetic measurements from TH-
417 E and TH-D (panels f2, g2). Prolonged plasma structure #7 has lower density of 4 - 9 cm^{-3} and
418 did not produce a notable compression effect in accordance with to TH-E magnetic
419 measurements (panel g2). It is important that inside each plasma structure, we reveal a dense
420 plasma core, which is characterized by enhanced speed of ~ 150 or ~ 220 km/s with a dominant
421 V_z component (negative or positive). These parameters, typical for plasma jets, formed pressure
422 of high magnitude, which exceeded the upstream solar wind pressure by 50-80 % (panel b2).
423 Likely, magnetosheath plasma jets interacted with the magnetopause, and then they were
424 partially trapped thereby penetrating into the magnetosphere (Dmitriev and Suvorova, 2015).
425 The amount of this penetrated plasma estimated by the authors can be comparable with estimates
426 of the total amount of plasma entering the dayside magnetosphere (Sibeck, 1999).

427 During the last time period 1658 - 1728 UT shown in panels (a3-g3), we have an excellent
428 opportunity to examine plasma parameters in the magnetosheath region adjacent to the
429 magnetopause. Panels (a3-f3) show two cases of magnetopause distortions followed by short
430 intervals of the magnetosheath from ~ 1700 to 1701 UT and from 1711 to ~ 1715 UT. The ULF
431 wave activity is also clearly seen in the magnetic measurement of the TH-E probe (panel g3).
432 The TH-D probe at distance of ~ 10.8 Re and ~ 13 LT suddenly crossed the magnetopause and
433 moved into the magnetosheath, a region where the magnetic field vector rotated to negative B_z
434 (panel f3). Plasma in both magnetosheath intervals has extremely high density (~ 20 cm^{-3}) and
435 high velocity (≤ 200 km/s). In the magnetosheath, one can see local pressure pulses around
436 ~ 1700 UT and ~ 1712 UT (lines #8 and 9). For #9 case, TH-E observed a small shallow hump of
437 the magnetic field of a few nT between two depletions at 1707 and 1715 UT (panel g3). The last



438 event (#10) shown in Figure 8c is a short penetration of magnetosheath plasma accompanied by
439 a small perturbation in the magnetospheric field observed at ~1724-1725 UT (panels e3, f3).
440 Density and pressure of this structure did not exceed the solar wind parameters, though the
441 velocity was large (~150 km/s) with dominant negative V_z component (panel b3-d3).

442 Thus, we found typical characteristics of dense and fast plasma jets in all intrusions of the
443 magnetosheath plasma into the magnetosphere and in the magnetosheath itself. Most of these
444 structures caused local compression effects at the dayside. Also, the TH-E magnetic field is
445 modulated by ULF waves in the range of magnetic pulsations Pc 3-4 with period between 10 and
446 60 seconds. As known, dayside Pc 3-4 waves are originated in the upstream solar wind and
447 penetrate into the magnetosphere, while their amplitude is controlled by a foreshock position or
448 IMF orientation (e.g., Guglielmi, 1974).

449 As shown in Figure 3, moderate auroral and polar cap activity was observed during the same
450 time (1600-1800 UT). However, it should be noted that in the preceded interval 1300-1600 UT,
451 associated with the deep electron injections and FEE enhancements, the THEMIS probes also
452 observed similar magnetic compression-expansion effects at inner part of orbits (~7 - 10 R_e). At
453 that time, we found enhanced magnetic activity in the polar cap (only in the northern
454 hemisphere), but no auroral activity. This raises an interesting question about spatial pattern of
455 geomagnetic field response to the impact of magnetosheath pressure pulses/plasma jets
456 interacting probably with the dayside magnetopause in the earlier interval 1300-1600 UT with
457 magnetic enhancements #1- #3.

458

459 **2.6. Global ground-based magnetic variations**

460 The global dynamics of geomagnetic field perturbations were studied using 1-min magnetic data
461 provided by an INTERMAGNET of ground magnetometers ([http://www.intermagnet.org/index-](http://www.intermagnet.org/index-eng.php)
462 [eng.php](http://www.intermagnet.org/index-eng.php)). Since there were no pressure pulses in the upstream solar wind and auroral activity was



463 low (see Figure 3), we expect that variations in the geomagnetic field (if any) should result from
464 the local magnetosheath pressure pulses. We used magnetic stations located at geomagnetic
465 latitudes below $\sim 60^\circ$ (Table 3), where a significant effect of different propagation time of
466 magnetohydrodynamic (MHD) waves in the magnetosphere will be almost hidden at 1 min
467 resolution. We grouped magnetic stations in meridional and latitudinal chains.

468 Figure 9 presents relative variations of horizontal (H) component, which was measured at
469 equatorial and low latitudes ranging from 0° to $\sim 20^\circ$ of geomagnetic latitude in the interval from
470 1100 to 1600 UT. In Figure 9, the stations are arranged in local time from morning to
471 postmidnight. The THEMIS magnetic field measurements are also shown at bottom. Four
472 magnetic field pulses of different amplitudes are seen around ~ 1200 , ~ 1335 - 1345 , ~ 1422 - 1430
473 and ~ 1545 - 1550 UT practically at all stations. The last three pulses correspond to those observed
474 by THEMIS at ~ 1334 , ~ 1421 and 1547 - 1550 UT (#1 - #3, see also Table 2). Moreover, one can
475 see the same pattern of magnetic variation “enhancement and decrease” in both ground-based
476 and satellite observations. Note that the first magnetic pulse at ~ 1200 UT can not be emerged
477 from THEMIS data because of the large background magnetic field in the inner magnetosphere.
478 Magnetic records at daytime and nighttime are clearly distinguished by amplitudes and time
479 delay relatively to the THEMIS data.

480 Magnetic records at nighttime stations (PHU, GZH, KNY, KDU, GUA, HON, PPT) are
481 characterized by prominent variations of H component, with peak-to-peak amplitudes of 3 - 5 nT.
482 The dayside stations (KOU, VSS, MBO, ASC, TSU, BNG, AAE, ABG) show relative weak, but
483 still distinguished, magnetic humps. Smaller amplitude at daytime is a result of an amplifying
484 integral effect from the Chapman-Ferraro current at the magnetopause and ionospheric Sq-
485 current at the ground.

486 It is interesting, that the magnetic pulse at 1200 UT is simultaneously (within the accuracy of ~ 1
487 min resolution) observed in all local time sectors. However, the other three enhancements were
488 observed in different LT sectors at slightly different time. A time difference varies from ~ 2 min



489 to ~10 min. The time delay depends on the time moment when a jet interacts with the
490 magnetopause in a given latitude-longitude sector (Dmitriev and Suvorova, 2012).

491 We draw attention to the fact that low-latitude HON and PPT stations, which were located in the
492 predawn sector (2-5 LT) from 1300 to 1500 UT, demonstrate the best coincidence (with a delay
493 of ~1 min) of magnetic enhancements #1 and #2 with those observed by THEMIS near noon.
494 Nighttime and daytime stations (PHU, GZH, KNY, KDU, GUA, MBO, ASC, TSU, BNG, AAE,
495 ABG) observed these peaks with ~3 - 5 min delay. The longest delay (~7 min) for pulses #1 and
496 #2 is found at morning/prenoon stations KOU and VSS (~9 - 11 LT).

497 As we have showed above, the FEE injections (F1 - F6 in Table 1) occur from ~2 to 5 LT. So,
498 we present meridional chains of stations in the predawn and midnight sectors (Figure 10). All
499 magnetic enhancements are well recognized from 0° to 60° of geomagnetic latitude. In midnight
500 and predawn sectors, the first magnetic pulse at ~1200 UT was observed practically
501 simultaneously everywhere. Magnetic pulse #1 around ~1333 UT was delayed by ~7 min at
502 midlatitudes (30°-60°) in the midnight sector (left panel) and by ~5 min in the predawn sector
503 (right panel). The pulse #2 shows a smaller delay (~3 min) at midlatitudes. The magnetic pulse
504 #3 at most stations in both sectors is observed around ~1545 UT, that is 2 min earlier than at TH-
505 E and 1 min later than at GOES (see Table 2). Thus, the low and middle latitude geomagnetic
506 observations in all local time sectors demonstrate that the magnetic variations of “enhancement-
507 decrease” pattern at 1200-1600 UT were observed by ground magnetometers as a global
508 phenomenon.

509

510 **3. Discussion and Summary**

511 In this work, using NOAA/POES and THEMIS satellites we investigated an unusual case of
512 deep injections of >30 keV electrons at $L < 1.2$ and associated FEE enhancements occurred
513 during quiet, nonstorm condition on August 1, 2008. A series of night injections of >30 keV



514 electrons could be associated with transient magnetospheric magnetic field perturbations. These
515 magnetic perturbations were observed globally like “compression-expansion” effects by
516 THEMIS and GOES 12 in the magnetosphere and by most of ground-based magnetometers from
517 INTERMAGNET network. Comparative analysis of the THEMIS, OMNI and ACE data showed
518 that the magnetic perturbations were caused by impact on the magnetopause by a series of
519 plasma pressure pulses propagated through the magnetosheath but not in the undisturbed
520 upstream solar wind. Such plasma jets are typical consequence of the foreshock dynamics driven
521 by variations in the IMF orientation (e.g., Lin et al., 1996) and are comprehensively studied
522 using THEMIS and MMS missions (e.g., Archer et al., 2012; 2013; Dmitriev and Suvorova,
523 2012; 2015; Plaschke et al., 2017). For our case, THEMIS measurements in the region in front of
524 the bow shock, showed obvious evidences of transient quasi-parallel bow shock and foreshock
525 conditions during the interval.

526 The strong FEE enhancements of intensity $\sim 10^{4-5} \text{ (cm}^2 \text{ s sr)}^{-1}$ were observed by POES in central
527 and eastern Pacific for a long time from ~ 1300 to 2300 UT. With analysis of longitudinal and
528 local time distributions of the enhancements we identified a series of night injections occurring
529 occasionally in the sector of 2-5 LT in the period from ~ 1300 to ~ 1700 UT (Figure 2). We found
530 that the injections of >30 keV electrons F1 - F6 (Table 1) occurred at much earlier time than the
531 weak auroral activity (1600 - 1800 UT), and hence, were unlikely related to it. The injections F8
532 and F10 occurred during the weak auroral activity interval. Also in that time, THEMIS-D
533 approached the magnetopause and detected magnetosheath plasma intrusions into the dayside
534 magnetosphere.

535 The quiet geomagnetic conditions in the period of 1300 - 1600 UT are consistent with
536 undisturbed solar wind conditions obtained from the OMNI data and ACE upstream monitor that
537 is not surprising. However, the picture, emerged from the THEMIS-C magnetic observations
538 right upstream of the subsolar bow shock at ~ 19 Re, showed an apparent discrepancy with
539 OMNI in the magnetic field structures (see Figure 5). For our case, the discrepancy appeared to



540 be due to an inability to predict accurately the evolution of small-scaled structures with quasi-
541 radial magnetic tubes during the propagation to the Earth and, as result, a notable uncertainty in
542 the time lag method applied in the OMNI database. Erroneous time lag is typical for cases of the
543 quasi-radial IMF orientation (e.g., Case and Wild, 2012; Mailyan et al., 2008; Bier et al., 2014;
544 Suvorova and Dmitriev, 2016). The actual solar wind parameters affecting the magnetosphere
545 were found to be related to a subsolar foreshock, which was observed by THEMIS. The analysis
546 of the THEMIS observations helps us to recognize possible external drivers, which might be
547 responsible for the deep FEE injections.

548 It is important to emphasize that only with OMNI data or with any far upstream monitor (ACE,
549 Wind, etc.), it would be impossible to resolve this unusual event. First, the OMNI data, as
550 mentioned above, present the upstream data modified by the timing procedure. But a problem of
551 the accuracy of time delays still exist as noted by a number of authors (e.g., Case and Wild, 2012;
552 McPherron et al., 2013; Mailyan et al., 2008). For example, the propagation time of magnetic
553 structures is determined less accurately for radial IMF condition (e.g., Bier et al., 2014;
554 Borovsky, 2008; Suvorova and Dmitriev, 2016). Second, there is a high probability that small-
555 scale magnetic field structures observed far upstream evolve unpredictably during the
556 propagation toward the Earth, so that the resulting structure can be different (e.g, Zastenker et al.,
557 2000; Borovsky, 2008). For example, the interval 1600 - 1800 UT is a good illustration for this,
558 proving no similarity exists in IMF cone angle variations in the solar wind and foreshock regions
559 (see Figure 5). Fortunately, we have a possibility to use more reliable information from the near
560 earth THEMIS mission on solar wind during the time period of interest.

561 During the period 1200 - 1800 UT, the magnetosphere was periodically under the quasi-radial
562 IMF conditions (Figure 5). The response of the magnetic field to these conditions was studied
563 with THEMIS located in the solar wind and magnetosphere and with ground-base
564 magnetometers of INTERMAGNET network. During the quasi-radial IMF intervals, THEMIS
565 observed intense ULF activity in the foreshock region. It is well known that the foreshock is also



566 accompanied by ULF waves observed inside the magnetosphere by satellites and ground based
567 magnetometers (e.g., Guglielmi, 1974; Clausen et al., 2009; Bier et al., 2014). However, the
568 amplitude of those magnetospheric ULF waves seems not strong enough to result in anomalous
569 radial transport of energetic electrons at $L < 1.2$.

570 The THEMIS measurements in the magnetosphere clearly show several local effects of
571 compression and expansion in the interval 1200 - 1600 UT (#1 - #3 in Table 2), and
572 magnetosheath plasma penetrations and magnetosheath encounters in the interval 1600 - 1800
573 UT (#4 - #10 in Table 2). The earlier interval, which is associated with several FEE injection
574 events, was investigated using ground magnetometer records. Signatures of magnetic variations
575 similar to the THEMIS observations were found in the H component at majority of ground
576 stations located from the geomagnetic equator to midlatitude (Figures 9 and 10). Common
577 feature for three magnetic pulses is that they were observed first at low latitudes in the
578 postmidnight/predawn sector (2-5 LT), and then their local time and latitudinal patterns become
579 quite different and complicated. Thus, the geomagnetic field responded globally to the local
580 pressure impacts compressing the dayside magnetosphere. At that, the postmidnight/predawn
581 sector (2-5 LT) shows the earliest pronounced response at low latitudes.

582 Analysis of the later interval 1600 - 1800 UT (Figure 7) indicated a possible cause of the
583 magnetic variations. Note that upstream bow shock conditions observed by TH-C during both
584 time intervals were similar in that the quasi-radial IMF appeared. During that time, THEMIS (D,
585 E) observed magnetic pulses, some of which were accompanied by penetrations of
586 magnetosheath plasma into the magnetosphere. THEMIS also encountered the magnetosheath
587 for a few minutes. Dense and high-speed plasma jets or pressure pulses were found in all plasma
588 structures, which penetrated into the magnetosphere or propagated in the magnetosheath (Figure
589 8). Obviously, impact of these magnetosheath plasma jets on the dayside magnetopause caused
590 compression effects in the magnetospheric field. This interval was accompanied by two FEE



591 injections F8 and F10 at 1633 and 1712 UT, respectively, which followed the magnetic pulses 4
592 - 8 occurred from 1614 to 1700 UT.

593 The magnetosheath pressure pulses or plasma jets arose during time intervals when quasi-radial
594 IMF tubes were passing the subsolar bow shock region as observed by THEMIS. The foreshock
595 was occasionally moving in or out of the subsolar region (see Figure 5). As the spacecraft
596 crossed an interface between two flux tubes, it observed a rotation discontinuity. Passages of the
597 rotational discontinuities followed by change between quasi-parallel and quasi-perpendicular
598 bow shock regimes created favorable conditions for generation of plasma jets (Lin et al., 1996).
599 Note that jets can be generated by directional discontinuities in absence of foreshock conditions
600 (cases #1 and #5) (Dmitriev and Suvorova 2012). THEMIS was able to observe directly such
601 plasma jets in the magnetosheath at later time, when it approached closely the magnetopause.
602 Similar effects of transient magnetospheric compression and expansion and their signatures at
603 low-latitude ground magnetometers were studied by Dmitriev and Suvorova (2012, 2015). As
604 they established, such magnetic field perturbations were caused by a pressure pulse impact of
605 magnetosheath plasma jet striking the dayside magnetopause during a foreshock transition
606 through the subsolar region toward flank.

607 Another important effect is penetration of the magnetosheath plasma into the magnetosphere at
608 low latitudes due to interaction of large-scale jets with the magnetopause (Dmitriev and
609 Suvorova, 2015). Recently, it was revealed that the magnetosheath high-speed jets result in
610 auroral brightening on the dayside (Han et al., 2017a; Wang et al., 2018). Sometimes, the aurora
611 penetrates to lower latitudes, so-called throat aurora. Han et al. (2017a) found that quasi-radial
612 IMF or subsolar foreshock condition is favorable for occurrence of dayside throat aurora,
613 whereas southward IMF has a weaker influence on its occurrence. Based on the comprehensive
614 study of properties of throat aurora, Han et al. (2018) concluded that throat auroras are definite
615 ground signatures for local magnetopause deformations and compressions produced by
616 magnetosheath plasma jet impact. They also provided direct evidence that the source of



617 precipitating particles in the throat auroras was the magnetosheath plasma (sometimes mixed
618 with magnetospheric plasma), which was effectively transported by jets from the magnetosheath
619 (Han et al., 2016; Han et al., 2017b). Thus, the jet impact is responsible for generating throat
620 aurora, which provides enhancements in auroral ionospheric conductivity on the dayside.

621 Dmitriev and Suvorova (2015) have found that the average rate of jet-related penetration of the
622 magnetosheath plasma into the magnetosphere is about 10^{29} particles per day. The penetrated hot
623 ions with energies of ~ 1 keV move quickly (within a few minutes) along the magnetic field lines
624 to high-latitude regions of the dayside ionosphere. We can estimate the flux of precipitating ions
625 of $\sim 10^7$ to 10^8 ($\text{cm}^2 \text{ s}^{-1}$) if we assume that particles precipitate on the dayside arc of 3° width at
626 70° latitude. Hence, we can assume that those ions can produce significant additional ionization
627 and increase conductivity of the high-latitude ionosphere on the dayside that induces an
628 enhancement of the electric field on the nightside and especially in the predawn sector, where the
629 conductivity is weak. The nightside electric field might penetrate from high to low latitudes and
630 produce ExB drift of electrons from the inner radiation belt to lower heights.

631 Thus, we can propose a scenario when magnetosheath plasma jets, associated with dynamical
632 subsolar foreshock and rotational discontinuities, interact with the dayside magnetopause and
633 cause compression effect with magnetic field perturbations and effective transport of the
634 magnetosheath plasma inside the magnetosphere. The magnetosheath plasma or mix with
635 magnetospheric plasma precipitates to the dayside ionosphere at high latitudes that result in a
636 local increase of the ionospheric conductivity. This in turn promotes generation of transient
637 localized electric fields, which are able to penetrate from high latitudes to very low latitudes (low
638 L-shells). Most favorable conditions for penetration of localized electric fields and FEE
639 enhancements arise in the period from May to September independently on geomagnetic activity
640 level (Suvorova, 2017). Our case event on 1 August 2008 corresponds well to these favorable
641 conditions.



642 Anomalous transport and loss of energetic particles in the magnetosphere was studied and
643 modeled in numerous papers (e.g., Glocer et al., 2011; Selesnick et al., 2016; Su et al., 2016;
644 Turner et al., 2015; Turner et al., 2017a; Zhao and Li, 2013; Zhao et al., 2017a). In the present
645 case, the magnetosphere is driven rather by plasma jets generated locally in the magnetosheath.
646 Moreover, we show that the solar wind conditions right upstream of the bow shock can be
647 substantially different from those measured in the far upstream regions. Another serious problem
648 is the generation/penetration of electric fields in the inner magnetosphere, which is far from
649 complete understanding. Numerical estimations show that the anomalous (fast) radial transport
650 of particles observed in the inner magnetosphere can be produced by the electric field up to 5
651 mV/m (Selesnick et al., 2016; Suvorova et al., 2013). At the present time, there are no models
652 predicting strong electric fields in the inner radiation belt and below. In this sense the scenarios
653 suggested here requires further development of new advanced models of the magnetosheath –
654 magnetosphere – ionosphere coupling.

Acknowledgements

The authors thanks a team of NOAA's Polar Orbiting Environmental Satellites for providing experimental data about energetic particles, the CDAWEB for providing the ACE solar wind data and Kyoto World Data Center for Geomagnetism (<http://wdc.kugi.kyoto-u.ac.jp/index.html>) for providing the geomagnetic indices. We thank the THEMIS team for magnetic and plasma data provided. The results presented in this paper rely on data collected at magnetic observatories. We thank the national institutes that support them and INTERMAGNET for promoting high standards of magnetic observatory practice (www.intermagnet.org). The OMNI data are provided by the GSFC/SPDF OMNIWeb platform (<http://cdaweb.gsfc.nasa.gov/>). The work was supported by grant MOST 106-2811-M-008-050 and MOST 106-2111-M-008-030-MY3 to National Central University.

References

- Archer, M. O., Horbury, T. S., and Eastwood, J. P.: Magnetosheath pressure pulses: Generation downstream of the bow shock from solar wind discontinuities, *J. Geophys. Res.*, 117, A05228, <https://doi.org/10.1029/2011JA017468>, 2012.
- Archer, M. O., Horbury, T. S., Eastwood, J. P., Weygand, J. M., and Yeoman, T. K.: Magnetospheric response to magnetosheath pressure pulses: A low-pass filter effect, *J. Geophys. Res.*, 118, 5454-5466, <https://doi.org/10.1002/jgra.50519>, 2013.



Asikainen, T., and Mursula, K.: Filling the South Atlantic anomaly by energetic electrons during a great magnetic storm, *Geophys. Res. Lett.*, 32, L16102, <https://doi.org/10.1029/2005GL023634>, 2005.

Auster, H. U., Glassmeier, K. H., Magnes, W., Aydogar, O., Baumjohann, W., Constantinescu, D., Fischer, D., Fornacon, K. H., Georgescu, E., Harvey, P., Hillenmaier, O., Kroth, R., Ludlam, M., Narita, Y., Nakamura, R., Okrafka, K., Plaschke, F., Richter, I., Schwarzl, H., Stoll, B., Valavanoglou, A., Wiedemann, M.: The THEMIS fluxgate magnetometer, *Space Sci. Rev.*, 141(1–4), 235–264, <https://doi.org/10.1007/s11214-008-9365-9>, 2008.

Bier, E. A., Owusu, N., Engebretson, M. J., Posch, J. L., Lessard, M. R., and Pilipenko V. A.: Investigating the IMF cone angle control of Pc3-4 pulsations observed on the ground, *J. Geophys. Res. Space Physics*, 119, 1797-1813, <https://doi.org/10.1002/2013JA019637>, 2014.

Borovsky, J. E.: Flux tube texture of the solar wind: Strands of the magnetic carpet at 1 AU? *J. Geophys. Res.*, 113, A08110, <https://doi.org/10.1029/2007JA012684>, 2008.

Dmitriev, A. V., and Suvorova, A. V.: Traveling magnetopause distortion related to a large-scale magnetosheath plasma jet: THEMIS and ground-based observations, *J. Geophys. Res.*, 117, A08217, <https://doi.org/10.1029/2011JA016861>, 2012.

Dmitriev, A. V., and Suvorova, A. V.: Large-scale jets in the magnetosheath and plasma penetration across the magnetopause: THEMIS observations, *J. Geophys. Res. Space Physics*, 120, 4423–4437, <https://doi.org/10.1002/2014JA020953>, 2015.

Dmitriev, A. V., and Yeh, H.-C.: Storm-time ionization enhancements at the topside low-latitude ionosphere, *Ann. Geophys.*, 26, 867-876, 2008.

Dmitriev, A. V., Suvorova, A. V., Klimenko, M. V., Klimenko, V. V., Ratovsky, K. G., Rakhmatulin, R. A., and Parkhomov, V. A.: Predictable and unpredictable ionospheric disturbances during St. Patrick's Day magnetic storms of 2013 and 2015 and on 8-9 March 2008, *J. Geophys. Res.: Space Physics*, 122, 2398-2432, <https://doi.org/10.1002/2016JA023260>, (2017).

Case, N. A., and Wild, J. A.: A statistical comparison of solar wind propagation delays derived from multispacecraft techniques, *J. Geophys. Res.*, 117, A02101, <https://doi.org/10.1029/2011JA016946>, 2012.

Crooker, N. U., Eastman, T. E., Frank, L. A., Smith, E. J., and Russell, C. T.: Energetic magnetosheath ions and the interplanetary magnetic field orientation, *J. Geophys. Res.*, 86, 4455-4460, 1981.

Glocer, A., Fok, M.-C., Nagai, T., Tóth, G., Guild, T., and Blake, J.: Rapid rebuilding of the outer radiation belt, *J. Geophys. Res.*, 116, A09213, <https://doi.org/10.1029/2011JA016516>, 2011.

Clausen, L. B. N., Yeoman, T. K., Fear, R. C., Behlke, R., Lucek, E. A., and Engebretson, M. J.: First simultaneous measurements of waves generated at the bow shock in the solar wind, the magnetosphere and on the ground, *Annales Geophysicae*, 27, 357-371, <https://doi.org/10.5194/angeo-27-357-2009>, 2009.

Gosling, J. T., Asbridge, J. R., Bame, S. J., Paschmann, G., and Scopke, N.: Observations of two distinct populations of bow shock ions in the upstream solar wind, *J. Geophys. Res.*, 5, 957–960, 1978.

Greenstadt, E. W., Russell, C. T., and Hoppe, M.: Magnetic field orientation and suprathermal ion streams in the earth's foreshock, *J. Geophys. Res.*, 85, 3473–3479, 1980.

Guglielmi, A.: Diagnostics of the magnetosphere and interplanetary medium by means of pulsations, *Space Sci. Rev.*, 16(3), 331–345, 1974.



Evans, D. S.: Dramatic increases in the flux of >30 keV electrons at very low L-values in the onset of large geomagnetic storms, *EOS Trans.*, 69(44), 1393, 1988.

Evans, D. S., and Greer, M. S.: Polar Orbiting Environmental Satellite Space Environment Monitor: 2. Instrument descriptions and archive data documentation. Tech. Memo. version 1.4, NOAA Space Environ. Lab., Boulder, Colo., 2004.

Heikkila, W. J.: Soft particle fluxes near the equator, *J. Geophys. Res.*, 76, 1076-1078, 1971.

Han, D.-S., Nishimura, Y., Lyons, L. R., Hu, H.Q., and Yang, H. G.: Throat aurora: The ionospheric signature of magnetosheath particles penetrating into the magnetosphere, *Geophysical Research Letters*, 43, 1819-1827, <https://doi.org/10.1002/2016GL068181>, 2016.

Han, D.-S., Hietala, H., Chen, X.-C., Nishimura, Y., Lyons R. L., Liu, J.-J., Hu, H.-Q., and Yang, H.-G.: Observational properties of dayside throat aurora and implications on the possible generation mechanisms, *J. Geophys. Res. Space Physics*, 122, 1853-1870, <https://doi.org/10.1002/2016JA023394>, 2017a.

Han, D.-S., Li, J.-X., Nishimura, Y., Lyons, L. R., Bortnik, J., Zhou, Liu, J. J., Hu, Z. J., Hu, H. Q., Yang, H. G., Fuselier, S. A., Le Contel, O., Ergun, R. E., Malaspina, D., Lindqvist, P. A., and Pollock, C.J.: Coordinated observations of two types of diffuse auroras near magnetic local noon by Magnetospheric Multiscale mission and ground all-sky camera, *Geophysical Research Letters*, 44(16), 8130-8139, <https://doi.org/10.1002/2017GL074447>, 2017b.

Han, D.-S., Liu, J.-J., Chen, X.-C., Xu, T., Li, B., Hu, Z.-J., Hu, H. Q., Yang, H. G., Fuselier, S. A., and Pollock, C.J.: Direct evidence for throat aurora being the ionospheric signature of magnetopause transient and reflecting localized magnetopause indentations. *J. Geophys. Res. Space Physics*, 123, 2658-2667, <https://doi.org/10.1002/2017JA024945>, 2018.

Imhof, W. L., Gaines, E. E., and Reagan, J. B.: Dynamic variations in intensity and energy spectra of electrons in the inner radiation belt. *J. Geophys. Res.*, 78(22), 4568–4577, 1973a.

Kikuchi, T. and Evans, D.S.: Energetic electrons observed by NOAA-6 over Japan (L=1.3) at the time of geomagnetic storm on February 8-9, 1986, *Proc. Res. Inst. Atmos., Nagoya University*, 36, 137-150, 1989.

King, J. H., and Papitashvili, N. E.: Solar wind spatial scales in and comparisons of hourly Wind and ACE plasma and magnetic field data, *J. Geophys. Res.*, 110, A02104, <https://doi.org/10.1029/2004JA010649>, 2005.

Krasovskii, V. I., Shklovski, I. S., Galperin, Yu. I., Svetlitskii, E. M., Kushnir, Yu. M., and Bordovskii, G. A.: The detection of electrons with energies of approximately 10 keV in the upper atmosphere (in Russian). *Iskusstvennye Sputniki Zemli*, 6, 113-126, (English translation: *Planet. Space Sci.*, 9, 27-40, 1962), 1961.

Lejosne, S., and Mozer, F. S.: Typical values of the electric drift $E \times B/B^2$ in the inner radiation belt and slot region as determined from Van Allen Probe measurements, *J. Geophys. Res. Space Physics*, 121, 12,014–12,024, <https://doi.org/10.1002/2016JA023613>, 2016.

Lin, Y., Lee, L. C., and Yan, M.: Generation of dynamic pressure pulses downstream of the bow shock by variations in the interplanetary magnetic field orientation, *J. Geophys. Res.*, 101, 479–493, 1996.

Lin, R. L., Zhang, X. X., Liu, S. Q., Wang, Y. L., and Gong, J. C.: A three-dimensional asymmetric magnetopause model. *J. Geophys. Res.*, 115, A04207, <https://doi.org/10.1029/2009JA014235>, 2010.

Mailyan, B., Munteanu, C., and Haaland, S.: What is the best method to calculate the solar wind propagation delay? *Ann. Geophys.*, 26, 2383–2394, 2008.



- Matsui, H., Torbert, R. B., Spence, H. E., Khotyaintsev, Yu. V., and Lindqvist, P.-A.: Revision of empirical electric field modeling in the inner magnetosphere using Cluster data, *J. Geophys. Res. Space Physics*, 118, 4119–4134, <https://doi.org/10.1002/jgra.50373>, 2013.
- McFadden, J. P., Carlson, C. W., Larson, D., Ludlam, M., Abiad, R., Elliott, B., Turin, P., Marckwordt, M., and Angelopoulos, V.: The THEMIS ESA plasma instrument and in-flight calibration, *Space Sci. Rev.*, 141, 277–302, <https://doi.org/10.1007/s11214-008-9440-2>, 2008.
- McIlwain, C. E.: Coordinates for mapping the distribution of magnetically trapped particles, *J. Geophys. Res.*, 66, 3681–3691, 1961.
- McPherron, R. L., Baker, D. N., Pulkkinen, T. I., Hsu, T. S., Kissinger, J., and Chu, X.: Changes in solar wind–magnetosphere coupling with solar cycle, season, and time relative to stream interface, *J. Atmos. Sol. Terr. Phys.*, 99, 1–13, <https://doi.org/10.1016/j.jastp.2012.09.003>, 2013.
- Park J., Min, K. W., Summers, D., Hwang, J., Kim, H. J., Horne, R. B., Kirsch, P., Yumoto, K., Uozumi, T., Lühr, H., and Green, J.: Non-stormtime injection of energetic particles into the slot region between Earth’s inner and outer electron radiation belts as observed by STSAT-1 and NOAA-POES, *Geophys. Res. Lett.*, 37, L16102, <https://doi.org/10.1029/2010GL043989>, 2010.
- Paschmann, G., Scokopke, N., Bame, N., Gosling, J.T., Russell, C.T., and Greenstadt, E.W.: Association of low-frequency waves with suprathermal ions in the upstream solar wind, *Geophys. Res. Lett.*, 6, 209–212, 1979.
- Paulikas, G. A.: Precipitation of particles at low and middle latitudes, *Rev. Geophys. Space Phys.*, 13(5), 709–734, 1975.
- Pfizer, K. A., and Winckler, J. R.: Experimental observation of a large addition to the electron inner radiation belt after a solar flare event, *J. Geophys. Res.*, 73(17), 5792–5797, 1968.
- Plaschke, F., Karlsson, T., Hietala, H., Archer, M., Voros, Z., Nakamura, R., Magnes, W., Baumjohann, W., Torbert, R. B., Russell, C. T., and Giles, B. L.: Magnetosheath high-speed jets: Internal structure and interaction with ambient plasma, *Journal of Geophysical Research: Space Physics*, 122, 10,157–10,175, 2017.
- Rowland, D. E., and Wygant, J. R.: Dependence of the large-scale, inner magnetospheric electric field on geomagnetic activity, *J. Geophys. Res.*, 103(A7), 14959–24964, 1998.
- Reeves, G. D., Friedel, R. H. W., Larsen, B. A., Skoug, R. M., Funsten, H. O., Claudepierre, S. G., Fennell, J. F., Turner, D. L., Denton, M. H., Spence, H. E., Blake, J. B., and Baker, D.N.: Energy-dependent dynamics of keV to MeV electrons in the inner zone, outer zone, and slot regions, *J. Geophys. Res.*, 121, 397–412, <https://doi.org/10.1002/2015JA021569>, 2016.
- Savenko, I. A., Shavrin, P. I., and Pisarenko, N. F.: Soft particle radiation at an altitude of 320 km in the latitudes near the equator (in russian). *Iskusstvennye Sputniki Zemli*, 13, 75–80 (English translation: *Planet. Space Sci.*, 11, 431–436, 1963), 1962.
- Schwartz, S. J., and Burgess, D.: Quasi-parallel shocks: A patchwork of three-dimensional structures, *Geophys. Res. Lett.*, 18, 373–376, 1991.
- Selesnick, R. S., Su, Y.-J., and Blake, J. B.: Control of the innermost electron radiation belt by large-scale electric fields, *J. Geophys. Res. Space Physics*, 121, 8417–8427, <https://doi.org/10.1002/2016JA022973>, 2016.
- Sibeck, D. G.: Plasma transfer processes at the magnetopause, *Space Sci. Rev.*, 88, 207–283, <https://doi.org/10.1023/a:1005255801425>, 1999.
- Su, Y.-J., Selesnick, R. S., and Blake, J. B.: Formation of the inner electron radiation belt by enhanced large-scale electric fields, *J. Geophys. Res. Space Physics*, 121, 8508–8522, <https://doi.org/10.1002/2016JA022881>, 2016.



Suvorova, A. V., and Dmitriev, A. V.: Radiation aspects of geomagnetic storm impact below the radiation belt, In V. P. Banks (Ed.), *Cyclonic and Geomagnetic Storms: Predicting Factors, Formation and Environmental Impacts*, (pp. 19-75), New York: NOVA Science Publishers, Inc., 2015.

Suvorova, A. V., and Dmitriev, A. V.: On magnetopause inflation under radial IMF, *Adv. Space Res.*, 58, 249-256, 2016.

Suvorova, A. V., Dmitriev, A.V., and Tsai, L.-C.: On relation between mid-latitude ionospheric ionization and quasi-trapped energetic electrons during 15 December 2006 magnetic storm, *Planet. Space Sci.*, 60, 363-369, <https://doi.org/10.1016/j.pss.2011.11.001>, 2012.

Suvorova, A. V., Dmitriev, A. V., Tsai, L.-C., Kunitsyn, V. E., Andreeva, E. S., Nesterov, I. A., and Lazutin, L. L.: TEC evidence for near-equatorial energy deposition by 30 keV electrons in the topside ionosphere, *J. Geophys. Res.*, 118, 4672–4695, <https://doi.org/10.1002/jgra.50439>, 2013.

Suvorova, A. V., Huang, C.-M., Matsumoto, H., Dmitriev, A. V., Kunitsyn, V. E., Andreeva, E. S., Nesterov, I. A., and Tsai, L.-C.: Low-latitude ionospheric effects of energetic electrons during a recurrent magnetic storm, *J. Geophys. Res. Space Physics*, 119, 9283-9303, <https://doi.org/10.1002/2014JA020349>, 2014.

Suvorova, A. V., Huang, C.-M., Dmitriev, A. V., Kunitsyn, V. E., Andreeva, E. S., Nesterov, I. A., Klimenko, M. V., Klimenko, V. V., and Tumanova, Yu. S.: Effects of ionizing energetic electrons and plasma transport in the ionosphere during the initial phase of the December 2006 magnetic storm, *J. Geophys Res.: Space Physics*, 121, 5880-5896, <https://doi.org/10.1002/2016JA022622>, 2016.

Suvorova, A.V.: Flux enhancements of >30 keV electrons at low drift shells $L < 1.2$ during last solar cycles, *J. Geophys Res.: Space Physics*, 122, 12274-12287, <https://doi.org/10.1002/2017JA024556>, 2017.

Tadokoro, H., Tsuchiya, F., Miyoshi, Y., Misawa, H., Morioka, A., and Evans, D. S.: Electron flux enhancement in the inner radiation belt during moderate magnetic storms, *Ann. Geophys.*, 25, 1359-1364, 2007.

Tanaka, Y., Nishino, M., and Iwata, A.: Magnetic storm-related energetic electrons and magnetospheric electric fields penetrating into the low-latitude magnetosphere ($L \sim 1.5$), *Planet. Space Sci.*, 38(8), 1051-1059, 1990.

Troshichev, O. A., Andrezen, V. G., Vennerstrøm, S., and Friis-Christensen, E.: Magnetic activity in the polar cap – A new index, *Planet. Space Sci.*, 36(11), 1095–1102, 1988.

Turner, D. L., Claudepierre, S. G., Fennell, J. F., O'Brien, T. P., Blake, J. B., Lemon, C., Gkioulidou, M., Takahashi, K., Reeves, G. D., Thaller, S., Breneman, A., Wygant, J. R., Li, W., Runov, A., and Angelopoulos, V.: Energetic electron injections deep into the inner magnetosphere associated with substorm activity, *Geophys. Res. Lett.*, 42, 2079-2087, <https://doi.org/10.1002/2015GL063225>, 2015.

Turner, D. L., Fennell, J. F., Blake, J. B., Claudepierre, S. G., Clemmons, J. H., Jaynes, A. N., Leonard, T., Baker, D. N., et al.: Multipoint observations of energetic particles injections and substorm activity during a conjunction between Magnetospheric Multiscale (MMS) and Van Allen Probes, *J. Geophys. Res. Space Physics*, 122, 11481-11504, <https://doi.org/10.1002/2017JA024554>, 2017a.

Turner, D. L., O'Brien, T.P., Fennell, J.F., Claudepierre, S. G., Blake, J. B., Jaynes, A. N., Baker, D. N., Kanekal, S., Gkioulidou, M., Henderson, M. G., and Reeves, G. D.: Investigating the source of near-relativistic and relativistic electrons in Earth's inner radiation belt, *J. Geophys. Res. Space Physics*, 122, 695-710, <https://doi.org/10.1002/2016JA023600>, 2017b.



Zastenker, G. N., Dalin, P. A., Petrukovich, A. A., et al.: Solar wind structure dynamics by multipoint observations, *Phys. Chem. Earth (C)*, 25 (1-2), 137-140, 2000.

Zhao, H., and Li, X.: Modeling energetic electron penetration into the slot region and inner radiation belt, *J. Geophys. Res. Space Physics*, 118, 6936-6945, <https://doi.org/10.1002/2013JA019240>, 2013.

Zhao, H., Li, X., Baker, D.N., Claudepierre, S.G., Fennell, J. F., Blake, J. B., Larsen, B. A., Skoug, R. M., Funsten, H. O., Friedel, R. H. W., Reeves, G. D., Spence, H. E., Mitchell, D. G., and Lanzerotti, L. J.: Ring current electron dynamics during geomagnetic storms based on the Van Allen Probes measurements, *J. Geophys. Res. Space Physics*, 121, 3333-3346, <https://doi.org/10.1002/2016JA022358>, 2016.

Zhao, H., Baker, D.N., Califf, S., Li, X., Jaynes, A. N., Leonard, T., Kanekal, S. G., Blake, J. B., Fennell, J. F., Claudepierre, S. G., Turner, D. L., Reeves, G. D., and Spence, H. E.: Van Allen Probes measurements of energetic particle deep penetration into the low L region ($L < 4$) during the storm on 8 April 2016, *J. Geophys. Res.*, 122, 12140-12152, <https://doi.org/10.1002/2017JA024558>, 2017a.

Zhao, H., Baker, D. N., Jaynes, A. N., Li, X., Elkington, S. R., Kanekal, S. G., Spence, H. E., Boyd, A. J., Huang, C.-L., and Forsyth, C.: On the relation between radiation belt electrons and solar wind parameters/geomagnetic indices: Dependence on the first adiabatic invariant and L^* , *J. Geophys. Res. Space Physics*, 122, 1624-1642, <https://doi.org/10.1002/2016JA023658>, 2017b.

Wang, B., Nishimura, Y., Heitala, H., Lyons, L., Angelopoulos, V., Plaschke, F., Ebihara, Y., and Weatherwax, A.: Impacts of magnetosheath high-speed jets on the magnetosphere and ionosphere measured by optical imaging and satellite observations, *J. Geophys. Res. Space Physics*, 123, 4879-4894, <https://doi.org/10.1002/2017JA024954>, 2018.



Table 1 *FEE Enhancements observed by POES satellites*

FEE ID #	POES s/c ID	Observed time hh:mm UT	Longitude deg	LT* h
F1	P8	12:50	-164.2	1.8
F2	P5	13:15	-128.8	5.1
F3	P6	13:53	-138.3	5.1
F4	P8	14:32	169.7	1.6
F5	P5	14:54	-152.7	5.1
F6	P6	15:34	-162.5	5.0
F7	P2	15:44	-98.7	9.3
F8	P5	16:33	-170.1	5.0
F9	P7	16:37	-107.3	9.7
F10	P6	17:12	180.0	4.9
F11	P2	17:24	-123.0	9.4
F12	P7	18:16	-131.0	9.8
F13	P2	19:06	-140.0	9.6
F14	P8	20:30	-105.0	13.8
F15	P6	23:09	-94.5	17.2

* Local time



Table 2 *Timing of Magnetic Field Enhancements and Plasma Pulses from THEMIS and GOES12*

ID #	s/c ID	Time of magnetic peak hh:mm:ss	Time of pressure pulse hh:mm:ss	Foreshock signatures
1	TH-D	13:33:40		absent
	TH-E	13:33:40		
	TH-B	13:33:40		
	G12	13:35:40		
2	TH-D	14:20:50		ions, ULF
	TH-E	14:20:50		
	TH-B	14:20:50		
	G12	14:20:50		
3	TH-D	15:50:30		ions, ULF
	TH-E	15:47:30		
	G12	15:44:00		
4	TH-D	16:14:05	~16:15 - 16:16	ions, ULF
	TH-E	16:14:05		
5	TH-D	16:38:20	16:40	absent
	TH-E	16:38:40		
6	TH-D	16:47:45	16:47:55	ions
	TH-E	16:47:45		
7	TH-D	-	16:51:22	ions, ULF
	TH-E	-		
8	TH-D	magnetosheath	17:00:25	ions, ULF
	TH-E	-		
9	TH-D	magnetosheath	~17:12 - 17:13	ions
	TH-E	17:12:30		
10	TH-D	17:24:50	17:24:50	ions, ULF
	TH-E	-		

**Table 3***Location of Magnetic Stations in Geographic and Geomagnetic coordinates*

Code	Name	GLat ^a	GLon ^a	MLat ^b	MLon ^b
AAE	Addis Ababa	9.0	38.8	5.3	109.9
ABG	Alibag	18.6	72.9	9.5	144.4
ASC	Ascension Island	-8.0	-14.4	-1.4	54.7
ASP	Alice Springs	-23.8	133.9	-34.1	-153.6
BNG	Bangui	4.3	18.6	4.6	89.3
CMO	College	64.9	-147.9	64.8	-102.6
CNB	Canberra	-35.3	149.4	-43.8	-134.5
CTA	Charters Towers	-20.1	146.3	-29.1	-140.7
EYR	Eyrewell	-43.4	172.4	-47.8	-107.0
GUA	Guam	13.6	144.9	4.2	-146.3
ZGH	Zhaoqing	23.0	112.5	11.7	-177.1
HON	Honolulu	21.3	-158.0	21.2	-92.7
KAK	Kakioka	36.2	140.2	26.2	-153.3
KDU	Kakadu	-12.7	132.5	-23.2	-156.3
KNY	Kanoya	31.4	130.9	20.7	-161.2
KOU	Kourou	5.2	-52.7	16.1	17.7
MBO	Mbour	14.4	-17.0	21.1	55.8
MCQ	McQuarie Island	-54.5	159.0	-60.9	-116.2
MMB	Memambetsu	43.9	144.2	34.2	-150.9
PET	Paratunka	53.0	158.3	45.6	-138.5
PHU	Phuthuy	21.0	106.0	9.7	176.0
PPT	Pamatai	-17.6	-149.6	-15.2	-76.5
SHU	Shumagin	55.4	199.5	54.1	-103.1
SIT	Sitka	57.1	-135.3	60.1	-83.7
TSU	Tsumeb	-19.2	17.6	-18.3	83.5
VSS	Vassouras	-22.4	-43.7	-12.1	24.6

^a Geographic latitude and longitude^b Magnetic latitude and longitude



FIGURE CAPTIONS

Figure 1. Geographic distribution of >30 keV electron fluxes measured by five NOAA/POES satellites on August 1, 2008 for the time interval (a) 0-12 UT, before the electron flux enhancements and (b) 12-24 UT, during the enhancements. In the forbidden zone, at low latitudes and equator, the quasi-trapped electron fluxes enhanced largely during nonstorm condition after 12 UT. The forbidden zone is bounded by $L=1.2$ (white lines) and located outside of the South Atlantic Anomaly (SAA) at equatorial-to-low latitudes. The solid black curve indicates the dip equator.

Figure 2. Locations of FEE enhancements in longitude and local time (black circles). Measurements within the SAA area are indicated by the open circles. Colorful curves denote low-latitude orbital passes of five NOAA/POES satellites: P2 (black), P5 (pink), P6 (red), P7 (blue), and P8 (green).

Figure 3. Solar wind parameters from OMNI data and geomagnetic indices on August 1, 2008. From top to bottom: (a) solar wind density (black) and dynamic pressure (blue), (b) solar wind speed, (c) interplanetary magnetic field (IMF) components B_x (blue), B_y (green), B_z (red) and magnitude B (black) in Geocentric Solar Magnetospheric (GSM) coordinates, (d) polar cap magnetic activity index PCN for northern (blue) and PCS for southern (red) hemispheres, (e) auroral electrojet index AE (black), AL (red), AU (green), and (f) storm time ring current variation index SYM-H. The shaded box denotes the time interval from 13 to 23 UT, when the nonstorm FEE enhancements were observed.

Figure 4. Spacecraft positions in GSM coordinates from 1200 to 1800 UT on August 1, 2018. The TH-C probe (blue) was in front of the subsolar bow shock. The TH-E (orange), TH-D (green), TH-B (brown), and GOES 12 (black) were located inside the dayside magnetosphere. The magnetopause position (black curve) was calculated using OMNI data for the upstream conditions at ~ 1600 UT following the model by Lin et al.'s (2010).

Figure 5. Observations of plasma and magnetic field on August 1, 2008. (a) Ion spectrogram (ion flux is in units of $\text{eV}/\text{cm}^2 \text{ s sr eV}$) and IMF vector components in GSM coordinates measured by TH-C, (b) IMF vector components from OMNI data set, (c) IMF cone angles plotted for TH-C (red) and OMNI (black).

Figure 6. Satellite measurements of magnetic field and plasma in the dayside magnetosphere and geomagnetic activity. (a) The B_z -GSM components from THEMIS probes TH-B (brown), TH-E (orange), and TH-D (green). The left y-axis corresponds to the magnetic measurements from TH-B and TH-D, and the right y-axis to TH-E. (b) The magnetic field strength from GOES-12 (black); (c) the SYM-H index; and (d) the ion spectrogram from TH-D (ion flux is in



units of $\text{eV/cm}^2 \text{ s sr eV}$). Dashed lines, numbered from 1 to 10, indicate time moments of magnetic and plasma disturbances observed by THEMIS.

Figure 7. Observations of plasma and magnetic field at 1530-1800 UT on August 1, 2008: (a-c) ion spectrograms measured by TH-C, TH-D, and TH-E (ion flux is in units of $\text{eV/cm}^2 \text{ s sr eV}$), (d) SYM-H index, (e) AE (black) and AL (red) indices, (f) horizontal magnetic field H_p detected by GOES 12 from 10 to 13 LT, (g) magnetic field strengths B_{tot} from TH-D (green) and TH-E (red), (h) IMF cone angles for TH-C (black) and for the ACE upstream monitor (blue). The ACE measurements are delayed by 60 min. Dashed lines and numbers #4 - #10 mark magnetospheric disturbances with magnetosheath ion population observed in the magnetosphere.

Figure 8. Observations of plasma and magnetic field during the intervals 1600 - 1630 UT, 1630 - 1700 UT and 1658 - 1728 UT on August 1, 2008. Panels show from top to bottom: (a) ion spectrogram from TH-D, (b) total pressure P_{tot} measured by the ACE upstream monitor (black) and TH-D (red), (c) plasma density D measured by ACE (black) and TH-D (blue), (d) TH-D measurements of bulk velocity V (black) and its components in GSM coordinates V_x (blue), V_y (green) and V_z (red), (e) transversal components of magnetic field B_x (blue) and B_y (green) from TH-D, (f) magnitude B and B_z component of magnetic field from TH-D, (g) magnitude B and B_z component of magnetic field from TH-E. The magnetosheath plasma penetration is denoted by dashed lines and numbers #4 - #10.

Figure 9. Relative variations in the horizontal component (H) of the geomagnetic field at low geomagnetic latitudes. Local time intervals are indicated near the station codes. The vertical lines depict time of the magnetic pulses at THEMIS (lines #1 - #3). Bottom panel shows magnetic field B measured by TH-E (orange) and by TH-D (green).

Figure 10. Relative variations in the horizontal component (H) of the geomagnetic field in the midnight (left) and predawn (right) sectors. The geomagnetic latitudes of the stations are indicated near station codes. The vertical lines depict time of the magnetic pulses at THEMIS.

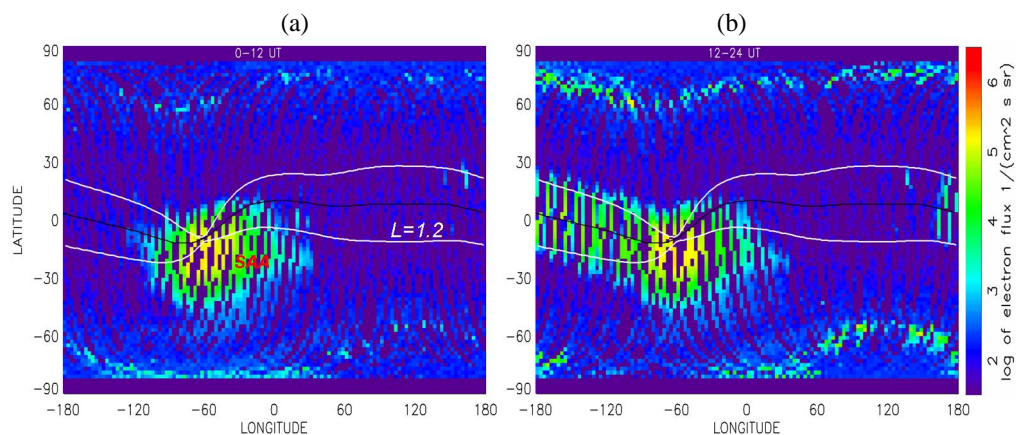


Figure 1. Geographic distribution of >30 keV electron fluxes measured by five NOAA/POES satellites on August 1, 2008 for the time interval (a) 0-12 UT, before the electron flux enhancements and (b) 12-24 UT, during the enhancements. In the forbidden zone, at low latitudes and equator, the quasi-trapped electron fluxes enhanced largely during nonstorm condition after 12 UT. The forbidden zone is bounded by $L=1.2$ (white lines) and located outside of the South Atlantic Anomaly (SAA) at equatorial-to-low latitudes. The solid black curve indicates the dip equator.

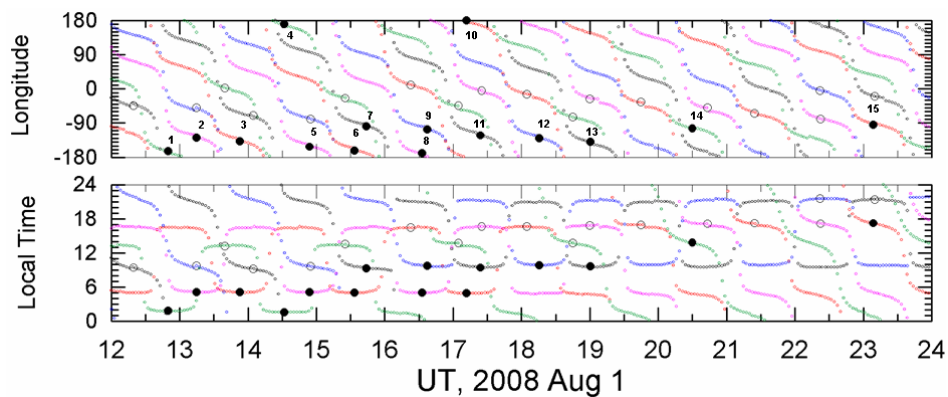


Figure 2. Locations of FEE enhancements in longitude and local time (black circles). Measurements within the SAA area are indicated by the open circles. Colorful curves denote low-latitude orbital passes of five NOAA/POES satellites: P2 (black), P5 (pink), P6 (red), P7 (blue), and P8 (green).

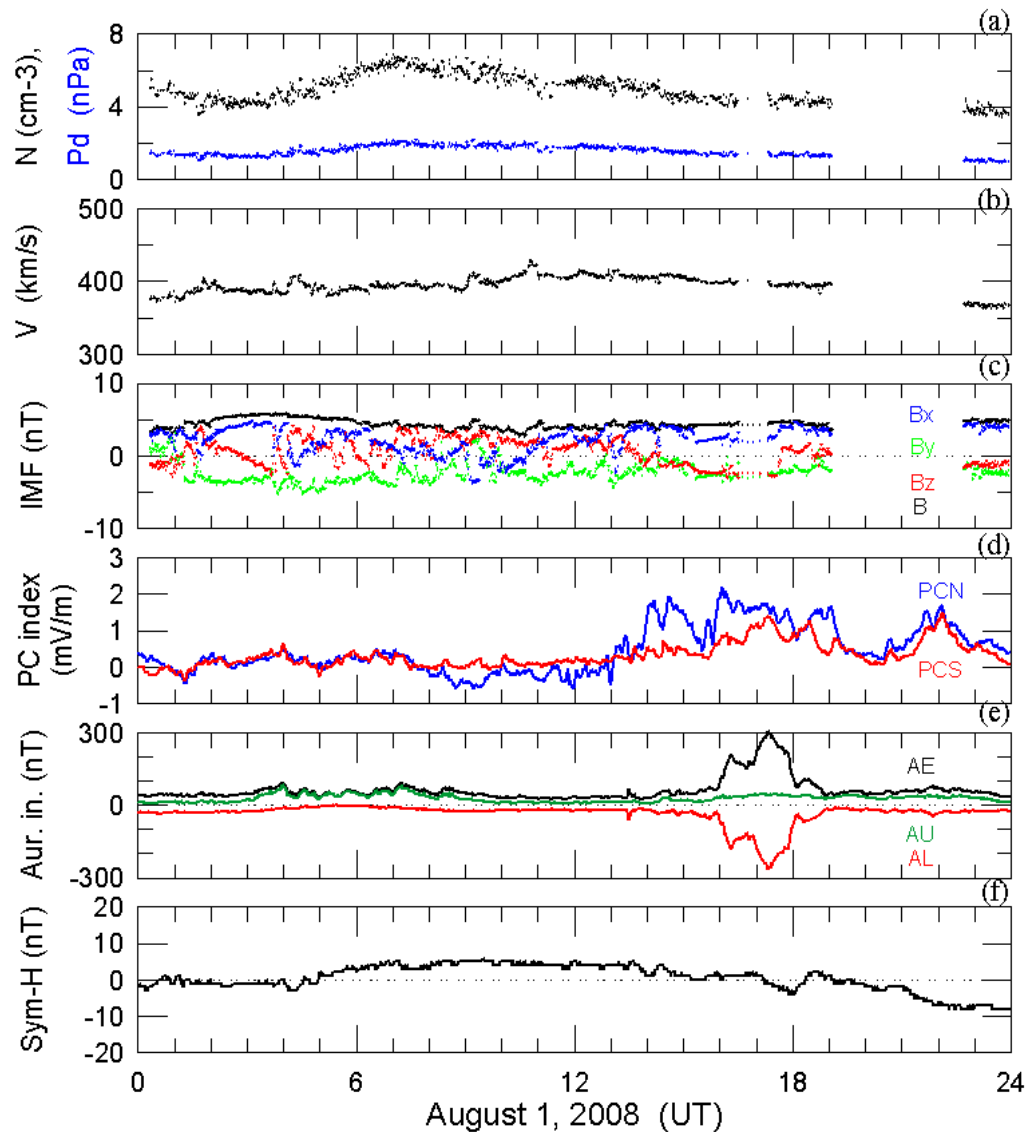


Figure 3. Solar wind parameters from OMNI data and geomagnetic indices on August 1, 2008. From top to bottom: (a) solar wind density (black) and dynamic pressure (blue), (b) solar wind speed, (c) interplanetary magnetic field (IMF) components Bx (blue), By (green), Bz (red) and magnitude B (black) in Geocentric Solar Magnetospheric (GSM) coordinates, (d) polar cap magnetic activity index PCN for northern (blue) and PCS for southern (red) hemispheres, (e) auroral electrojet index AE (black), AL (red), AU (green), and (f) storm time ring current variation index SYM-H. The shaded box denotes the time interval from 13 to 23 UT, when the nonstorm FEE enhancements were observed.

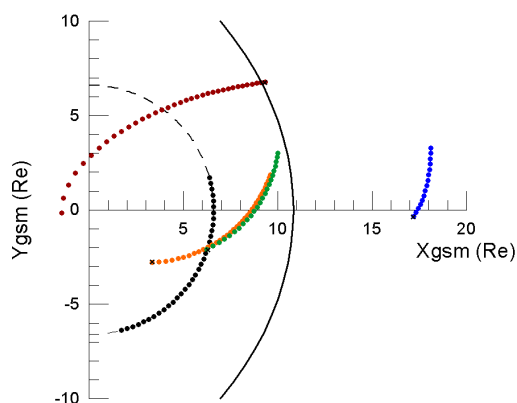


Figure 4. Spacecraft positions in GSM coordinates from 1200 to 1800 UT on August 1, 2018. The TH-C probe (blue) was in front of the subsolar bow shock. The TH-E (orange), TH-D (green), TH-B (brown), and GOES 12 (black) were located inside the dayside magnetosphere. The magnetopause position (black curve) was calculated using OMNI data for the upstream conditions at ~1600 UT following the model by Lin et al.'s (2010).

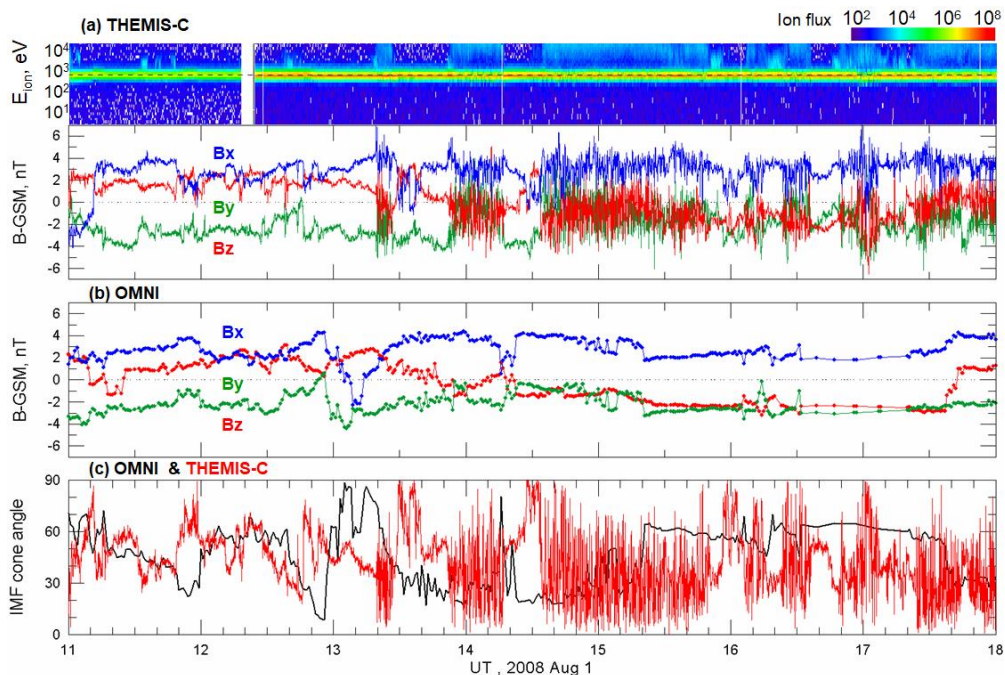


Figure 5. Observations of plasma and magnetic field on August 1, 2008. (a) Ion spectrogram (ion flux is in units of eV/cm² s sr eV) and IMF vector components in GSM coordinates measured by TH-C, (b) IMF vector components from OMNI data set, (c) IMF cone angles plotted for TH-C (red) and OMNI (black).

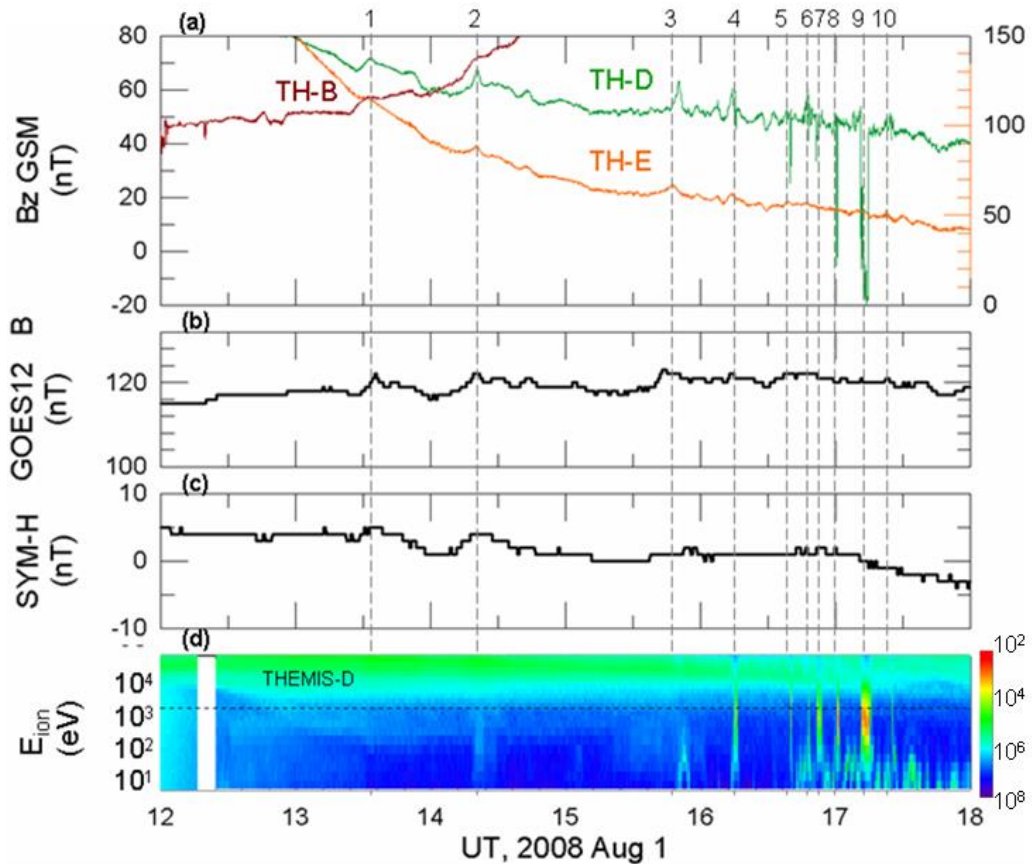


Figure 6. Satellite measurements of magnetic field and plasma in the dayside magnetosphere and geomagnetic activity. (a) The B_z -GSM components from THEMIS probes TH-B (brown), TH-E (orange), and TH-D (green). The left y-axis corresponds to the magnetic measurements from TH-B and TH-D, and the right y-axis to TH-E. (b) The magnetic field strength from GOES-12 (black); (c) the SYM-H index; and (d) the ion spectrogram from TH-D (ion flux is in units of $\text{eV}/\text{cm}^2 \text{ s sr eV}$). Dashed lines, numbered from 1 to 10, indicate time moments of magnetic and plasma disturbances observed by THEMIS.

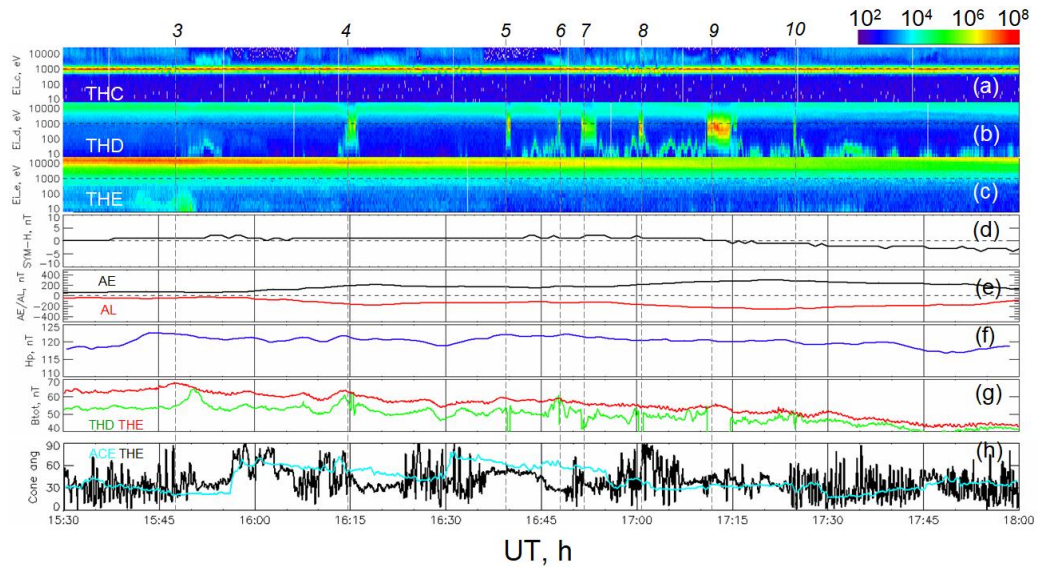


Figure 7. Observations of plasma and magnetic field at 1530-1800 UT on August 1, 2008: (a-c) ion spectrograms measured by TH-C, TH-D, and TH-E (ion flux is in units of $\text{eV}/\text{cm}^2 \text{ s sr eV}$), (d) SYM-H index, (e) AE (black) and AL (red) indices, (f) horizontal magnetic field H_p detected by GOES 12 from 10 to 13 LT, (g) magnetic field strengths B_{tot} from TH-D (green) and TH-E (red), (h) IMF cone angles for TH-C (black) and for the ACE upstream monitor (blue). The ACE measurements are delayed by 60 min. Dashed lines and numbers #4 - #10 mark magnetospheric disturbances with magnetosheath ion population observed in the magnetosphere.

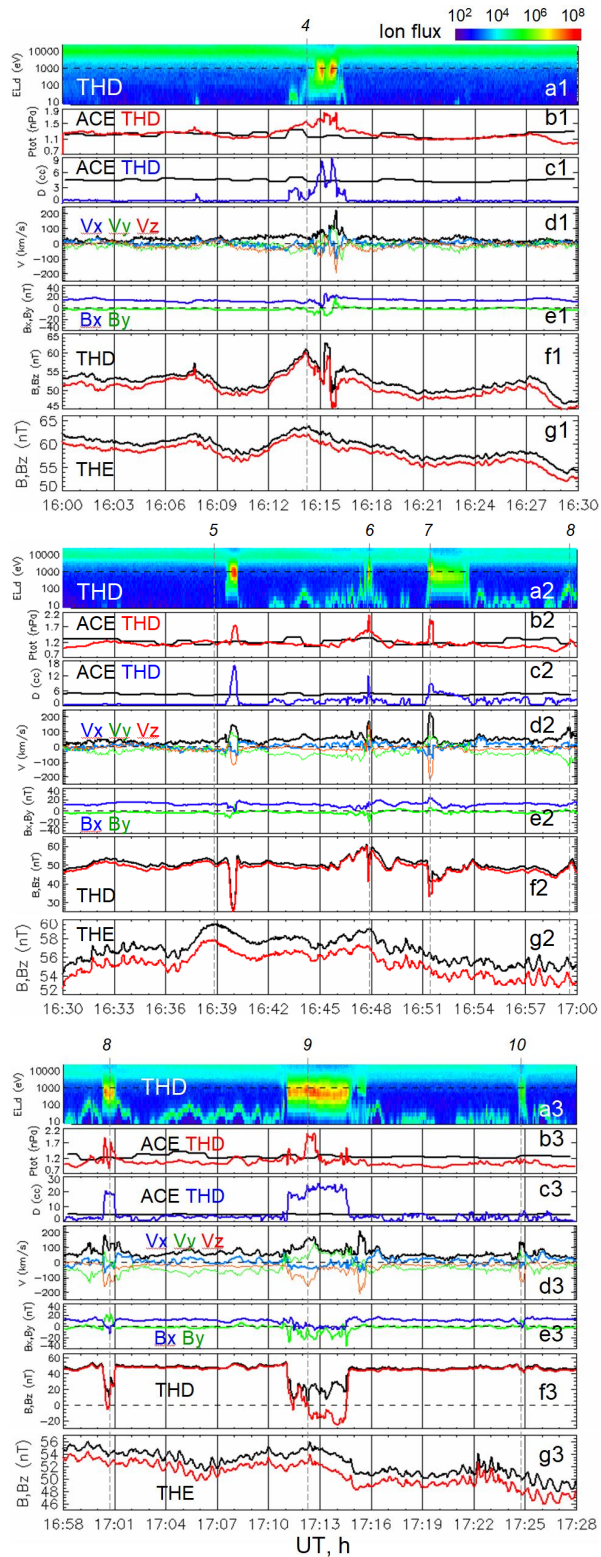




Figure 8. Observations of plasma and magnetic field during the intervals 1600 - 1630 UT, 1630 - 1700 UT and 1658 - 1728 UT on August 1, 2008. Panels show from top to bottom: (a) ion spectrogram from TH-D, (b) total pressure measured by the ACE upstream monitor (black) and TH-D (red), (c) plasma density measured by ACE (black) and TH-D (blue), (d) TH-D measurements of bulk velocity V (black) and its components in GSM coordinates V_x (blue), V_y (green) and V_z (red), (e) transversal components of magnetic field B_x (blue) and B_y (green) from TH-D, (f) magnitude B and B_z component of magnetic field from TH-D, (g) magnitude B and B_z component of magnetic field from TH-E. The magnetosheath plasma penetration is denoted by dashed lines and numbers #4 - #10.

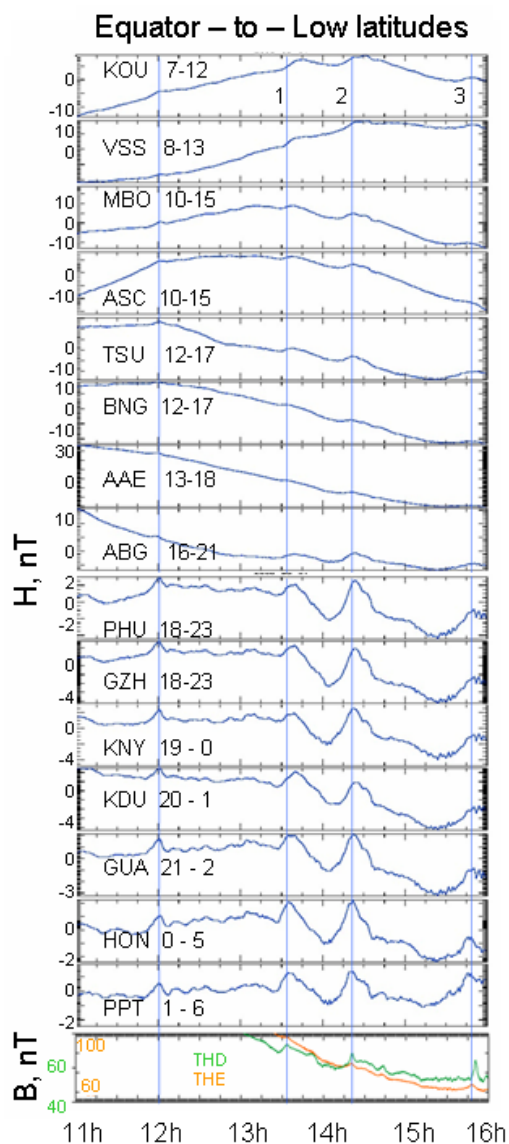


Figure 9. Relative variations in the horizontal component (H) of the geomagnetic field at low geomagnetic latitudes. Local time intervals are indicated near the station codes. The vertical lines depict time of the magnetic pulses at THEMIS (lines #1 - #3). Bottom panel shows magnetic field B measured by TH-E (orange) and by TH-D (green).

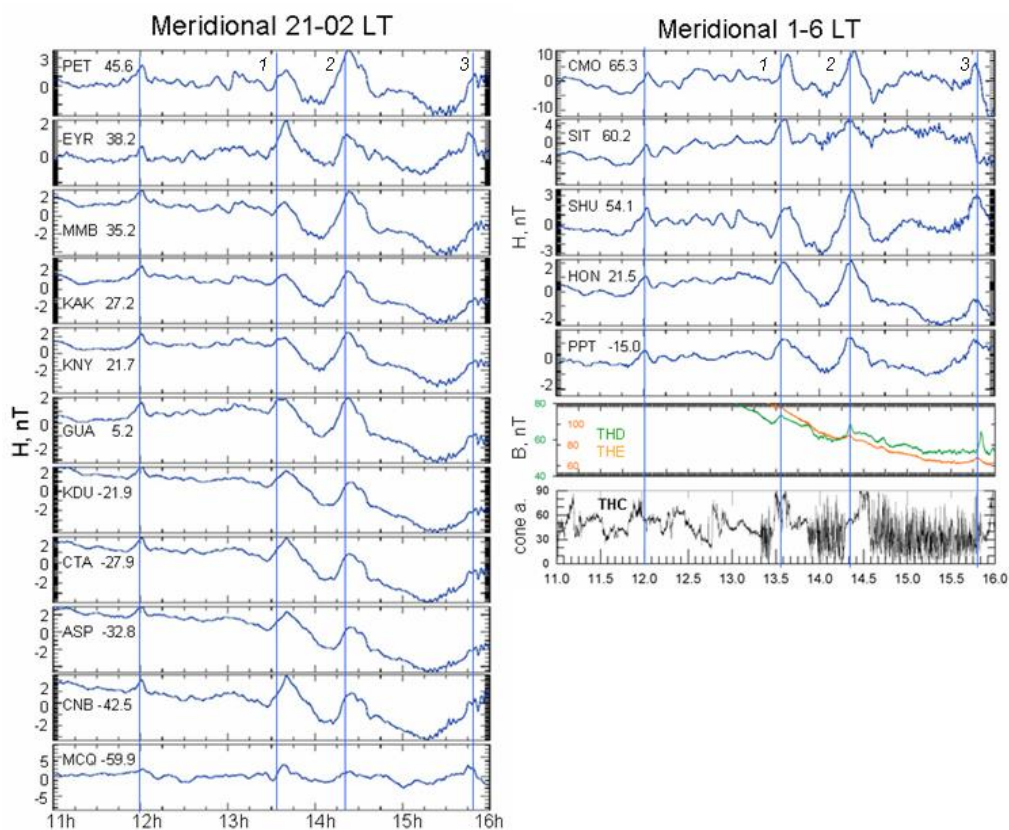


Figure 10. Relative variations in the horizontal component (H) of the geomagnetic field in the midnight (left) and predawn (right) sectors. The geomagnetic latitudes of the stations are indicated near station codes. The vertical lines depict time of the magnetic pulses at THEMIS.